



Characterization of Cu-5Fe (wt.%) fabricated by powder consolidation using high-pressure torsion

Amar Djemli^{1,2}, Hiba Azzeddine^{3,*}, Piotr Bazarnik⁴, Foudil Sahnoune¹, Yi Huang⁵, Thierry Baudin⁶, François Brisset⁶, Megumi Kawasaki⁷, and Terence G. Langdon⁸

¹ Physics and Chemistry of Materials Lab, Faculty of Sciences, University of M'sila, University Pole, Road Bourdj Bou Arreiridj, 28000 M'sila, Algeria

² Department of Chemistry, Faculty of Sciences, University of M'sila, University Pole, Road Bourdj Bou Arreiridj, 28000 M'sila, Algeria

³ Laboratory of Materials and Renewable Energy, Faculty of Sciences, University of M'sila, University Pole, Road Bourdj Bou Arreiridj, 28000 M'sila, Algeria

⁴ Faculty of Materials Science and Engineering, Warsaw University of Technology, Woloska 141, 02-507 Warsaw, Poland

⁵ Department of Design and Engineering, Faculty of Science and Technology, Bournemouth University, Poole, Dorset BH12 5BB, UK

⁶ CNRS, Institut de Chimie Moléculaire et des Matériaux d'Orsay, Université Paris-Saclay, 91405 Orsay, France

⁷ School of Mechanical, Industrial and Manufacturing Engineering, Oregon State University, Corvallis, OR 97331, USA

⁸ Departments of Aerospace & Mechanical Engineering and Materials Science, University of Southern California, Los Angeles, CA 90089-1453, USA

Received: 17 June 2025

Accepted: 10 September 2025

© The Author(s), under exclusive licence to Springer Science+Business Media, LLC, part of Springer Nature, 2025

ABSTRACT

Bulk pure Cu and Cu-5Fe (wt%) materials were successfully fabricated at room temperature by powder consolidation using high-pressure torsion (HPT) processing through 30 turns under a pressure of 6 GPa. The microstructure, texture and mechanical properties of the fabricated bulk discs were systematically characterized across their diameters using electron backscatter diffraction, scanning electron microscopy, transmission electron microscopy, X-ray diffraction and Vickers microhardness. Additionally, their thermal stability was evaluated after annealing treatment at 500 °C for 6 h. The results show that two grain refinement stages occurred in the Cu disc accompanied by the formation of partial *A*-fibre (A_1^*/A_2^* and *A* components). The dynamic recrystallization was delayed in the Cu-5Fe disc owing to the pinning effect of Fe content. Consequently, the grain refinement was more effective, and the texture gradually developed the *B*, *A* and A_1^* components. The Cu-5Fe disc was harder than the Cu disc, and the microhardness increased across the disc diameter. Rapid grain growth with a high amount of Cu₂O oxide and retained texture were the main characteristics of the annealed Cu disc. The precipitation of Fe phase during annealing led to the development of a duplex

Handling Editor: Nima Haghddadi.

Address correspondence to E-mail: hiba.azzeddine@univ-msila.dz

<https://doi.org/10.1007/s10853-025-11534-w>

Published online: 24 September 2025

microstructure at the centre and mid-radius positions and a stable microstructure at the edge of the Cu-5Fe disc. Eventually, the annealing texture was transformed into a complete *A*-fibre (A_1^*/A_2^* and A/\bar{A} components) which was quite similar to the Cu disc. The microhardness decreased after annealing but it was more homogeneously distributed across the disc diameter than the HPT-processed disc. The results were discussed based on the different grain refinement mechanisms, static recrystallization mechanisms, solute elements, dislocations and annealing twins.

Introduction

The association of high thermal conductivity and electrical conductivity of copper (Cu) with the soft magnetic properties and high strength of iron (Fe) by forming Cu-Fe alloys is of great potential interest in applications in high-precision technology fields [1]. However, according to the phase diagram, the Fe-Cu system is fully immiscible in the solid state, making the preparation of Cu-Fe alloys through traditional casting often challenging, especially with high Fe content (> 5 wt.%). In fact, the segregation of the Fe phase and the high Fe content in the solid solution can cause a serious microstructural inhomogeneity and decrease the electrical conductivity and the strength of the alloy, thereby restricting the broader application of Cu-Fe alloys [2–4].

Considerable efforts have been made over the past years to develop new material manufacturing routes, including rapid solidification [5], mechanical alloying [6] and a strong magnetic field [7] methods to control the Fe solubility in the Cu matrix, morphology and volume fraction of the Fe phase. Concurrently, other research has focussed on the impact of additional alloying elements in order to produce a uniform microstructure and obtain simultaneous high mechanical and electrical performances of Cu-Fe alloys [8–11]. For example, it was found that the addition of Si and Mg solutes has the ability to reduce the segregation and refine the Fe phase, which is a remarkable advantage for boosting the strength and electrical conductivity of the Cu-Fe alloys [8, 9].

Thermomechanical processing is an effective procedure for tailoring the grain size of the Cu matrix and the size, morphology and distribution of the Fe phase in Cu-Fe alloys [12–18]. However, the results indicate that the microstructures are highly sensitive regarding the deformation and ageing conditions such as strain level and temperature [13, 14, 19]. At present, severe plastic deformation (SPD) processing is an emerging tool for the production of bulk ultrafine-grained

materials with enhanced mechanical and functional properties which result from the creation of high densities of lattice defects such as dislocations, vacancies and grain boundaries by using high plastic strains [20]. Among SPD techniques, high-pressure torsion (HPT) processing can introduce outstanding grain refinement (at the nanometer scale) as well as promote phase transformations, such as decomposition or dissolution of phases and even amorphization [21, 22]. In addition, the fabrication of bulk materials by powder consolidation and mechanical bonding chips is easily achieved by HPT processing at room temperature owing to the simultaneous application of a high hydrostatic pressure and torsional shear strain [23–26]. Therefore, many works report the successful feasibility of HPT processing for fabricating Cu-Fe alloys [27–33]. Nevertheless, the deformation behaviour and the evaluation of the relationship between microstructure, crystallographic texture and mechanical properties of HPT-processed Cu-Fe alloys remain limited [31, 33].

In the current work, bulk Cu-xFe ($x = 0$ and 5 wt%) alloys were successfully fabricated at room temperature (RT) by powder consolidation using HPT processing through 30 turns under a pressure of 6 GPa. The evolution of microstructure, texture and microhardness across the disc diameters was characterized using different experimental techniques, including electron backscatter diffraction (EBSD), scanning electron microscopy (SEM), transmission electron microscopy (TEM), X-ray diffraction (XRD) and Vickers microhardness. Further, the static recrystallization behaviour of the HPT-processed discs was evaluated after annealing at 500 °C for 6 h.

Materials and experimental procedures

The starting materials used in the present study were commercial copper (99.9% purity) and iron (99.9% purity) powders with average particle sizes of 25

and 36 μm , respectively. The powder mixtures with an elemental composition of 5 wt.% Fe and 95 wt.% Cu were thoroughly prepared by hand mixing using a mortar and pestle under ambient conditions for 60 min and dispersed by ultrasound treatment for 15 min using a probe sonicator operated at a frequency of 40 kHz to break up any loose agglomerates and increase the uniformity of the mixture. The mixture was pre-compactated at RT using a hand-press machine into a disc shape with a 10 mm diameter and 1 mm thickness with an applied pressure of 450 MPa. Then, the discs were consolidated at RT using the HPT processing for 30 turns under a rotation rate of 1 rpm and a pressure of 6 GPa. Based on the existing literature [28, 31, 32], it is believed that such large torsional turns (30 turns) and high applied pressure (6 GPa) would be sufficient to produce a consolidated Cu-Fe material with homogeneous nanostructure.

The HPT processing was conducted under quasi-constrained conditions [34] to restrict the outward flow of material around the periphery of the disc during the processing operation. Precautions were taken throughout the HPT processing to avoid slippage between the disc sample and anvils [35]. Furthermore, the temperature rise during HPT processing is relatively low, which will not have a subsequent effect on the development of microstructure and texture [36].

The deformed discs were then subjected to annealing treatment at 500 °C for 6 h in a radiation furnace, followed by air quenching. The selection of the heat treatment condition was based on prior studies, which indicated that the optimal ageing temperature of Cu-Fe alloys is typically around 500 °C [1].

The discs were cut into two halves along their mid-plane. As illustrated in Fig. 1, the microstructural observations, texture and microhardness measurements were performed on the cross-sectional (CD-SD) planes of the HPT-processed and annealed discs. For information, the shear reference frame is defined as the shear direction (SD), radial direction (RD) and compression direction (CD).

It should be noted that when the number of HPT turns was above 5 turns, there was no recovery or self-annealing at RT during the storage time of the HPT-processed pure Cu [37].

The EBSD measurements were performed near the centre ($r \sim 0.2 \text{ mm}$), at the mid-radius position ($r \sim 2.5 \text{ mm}$) and the edge ($r \sim 4.5 \text{ mm}$) of the mid-thickness plane of the HPT-processed and annealed discs (see Fig. 1) using a TSL-EDAX-Hikari system mounted

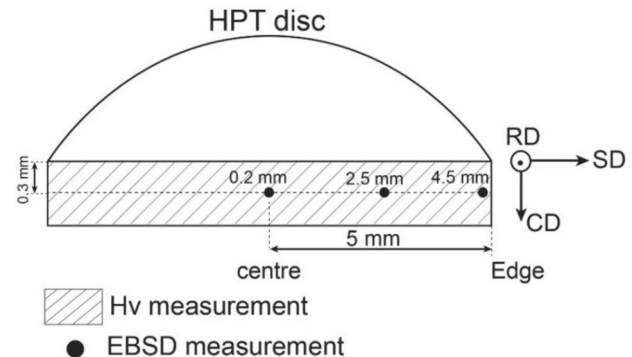


Figure 1 Schematic illustration indicating the positions for the EBSD and microhardness measurements on the vertical cross section of the HPT disc. SD, CD and RD are the coordinate systems.

on a scanning electron microscope (FEG-SEM ZEISS Supra 55 VP) operating at 20 kV. Sample preparation for the EBSD measurements consisted of mechanical polishing using SiC abrasive papers up to 4000-grid, followed by diamond polishing up to 0.25 μm and then a final polishing using oxide polishing suspensions (OPS).

Data collected from scanned areas of $25 \times 25 \mu\text{m}^2$ with a 25 nm step size were treated by the Orientation Imaging Microscopy OIM™ software. The scanned areas for the annealed Cu discs were $50 \times 50 \mu\text{m}^2$ with a step size of 50 nm. A grain tolerance angle of 5°, a minimum grain size of 5 pixels and a confidence index (CI) < 0.05 were chosen as a clean-up procedure for the quantitative EBSD analyses. The grain boundaries were classified into sub-grain boundaries with misorientations $2^\circ < \theta < 5^\circ$, low-angle grain boundaries (LAGBs) with misorientations $5^\circ < \theta < 15^\circ$ and high-angle grain boundaries (HAGBs) with $\theta > 15^\circ$. Grain boundaries with misorientation angles $\theta < 2^\circ$ were removed to avoid spurious boundaries caused by orientation noise.

The dynamically recrystallized fraction in the HPT-processed discs was estimated using the grain orientation spread (GOS) approach implemented in the OIM™ software, where the GOS is known as the mean deviation between the orientation of each point in the grain and the mean orientation of the grain [38]. In the present case, grains with GOS $< 1^\circ$ are assumed to be completely recrystallized [38].

The kernel average misorientation (KAM) approach was used to estimate the stored energy, E_s ,

originating from the geometrically necessary dislocation (GNDs), following the equation [39]:

$$E_s = \frac{\alpha \mu b \theta_{KAM}}{2nd} \quad (1)$$

where α is a parameter that depends on the grain boundary type with values of 2 and 4 for pure tilt and twist boundaries, respectively [40], $\mu = 48.3$ GPa is the shear modulus for Cu [39], $b = 0.255$ nm is the magnitude of the Burgers vector for Cu [39], θ_{KAM} is the average misorientation angle, $n = 3$ for the nearest neighbour and $d = 25$ nm is the EBSD scan step size. In the present case, the θ_{KAM} value was calculated from the average misorientation angle between the point and its 3rd neighbour ($n = 3$) excluding misorientations greater than 5° .

The texture was quantified using toolbox MTEX by calculating the orientation distribution function (ODF) using the harmonic method ($L = 22$) and a Gaussian function with a half-width of 5° to model each orientation [41].

A scanning electron microscope (SEM), Hitachi SU8000, operating at an accelerating voltage of 10 kV in backscattered electron (BSE) mode and equipped with an energy-dispersive spectrometer (EDS), was used to identify the chemical elements of various phases present near the mid-radius position of the HPT-processed Cu-5Fe disc. Specimens for SEM were prepared via grinding and ion polishing on Hitachi Ion Milling System IM-4000. The ion milling is a damage-less process, so that the polishing with the ion beam eliminates all deformation, stresses and oxide layers. Moreover, the surface quality is sufficiently good that the structure of such prepared joints can be observed on an SEM microscope through the channelling contrast.

Detailed structural investigations were further carried out using a Thermo Fisher Scientific SPEC-TRA 200 scanning transmission electron microscope (STEM), featuring a dedicated Cs-corrected high-resolution system operating at an accelerating voltage of 200 kV and achieving a spatial resolution of 75 pm. Chemical analyses were performed using a next-generation Super-X EDX system, equipped with four state-of-the-art detectors, each offering an increased collection solid angle of 0.7 sr. STEM samples were extracted from the mid-radius region of the discs using a gallium focused ion beam (FIB) microscope (Hitachi NB-5000), following a standard cutting procedure [42].

The X-ray diffraction (XRD) patterns were recorded on the RD-SD plane of the discs using an X'PERT PRO MPD diffractometer operating at 40 kV and 40 mA with Cu-K radiation ($\lambda = 0.1541$ nm). The data were collected over a range of $2\theta = 10\text{--}80^\circ$ with a step size of 0.02° .

Vickers microhardness measurements were taken using a Mitutoyo HM-200 with a load of 50 gf and a dwell time of 10 s. The discs were cut vertically across the diameters and the cross sections were polished to mirror-like surfaces. A series of hardness values were recorded on these cross sections, measuring $8000 \times 450 \mu\text{m}^2$, where a rectilinear grid pattern (see Fig. 1), having 150 μm separation between adjacent points, was applied for the automated measurement procedure. The recorded hardness values gave a total of 248 points, and these points were used for the construction of color-coded contour maps.

Results

XRD and SEM characterization

Figure 2 presents the XRD patterns of the HPT-processed and annealed Cu and Cu-5Fe discs. Both HPT-processed Cu (Fig. 2a) and Cu-5Fe (Fig. 2b) discs exhibit peaks belonging only to the Cu matrix. This indicates the possible formation of a solid solution state in the HPT-processed Cu-5Fe disc. For confirmation, Fig. 3 displays the SEM images with different magnifications and EDS analysis taken near the mid-radius position of the HPT-processed Cu-5Fe disc. For comparison, an SEM photograph showing the microstructure near the mid-radius of the HPT-processed Cu disc is displayed in Fig. 3c. It can be observed that the formation of the granular microstructure is decorated by numerous black zones of different sizes.

The EDS analysis of point 1 demonstrates the formation of a solid solution containing almost 5% of Fe element (Fig. 3b). The presence of high content of Fe ($74.4 \pm 0.7\%$) and O ($22.5 \pm 0.2\%$) elements in the black zone (Point 2) indicated the formation of the iron oxide (Fe_2O_3) phase.

The absence of peaks belonging to the Fe_2O_3 phase in the XRD pattern of the HPT-processed Cu-5Fe disc may indicate the low fraction of this phase. As shown in Fig. 3c, a granular microstructure is also reached for the HPT-processed Cu disc. The microstructure is decorated by black spots homogeneously distributed,

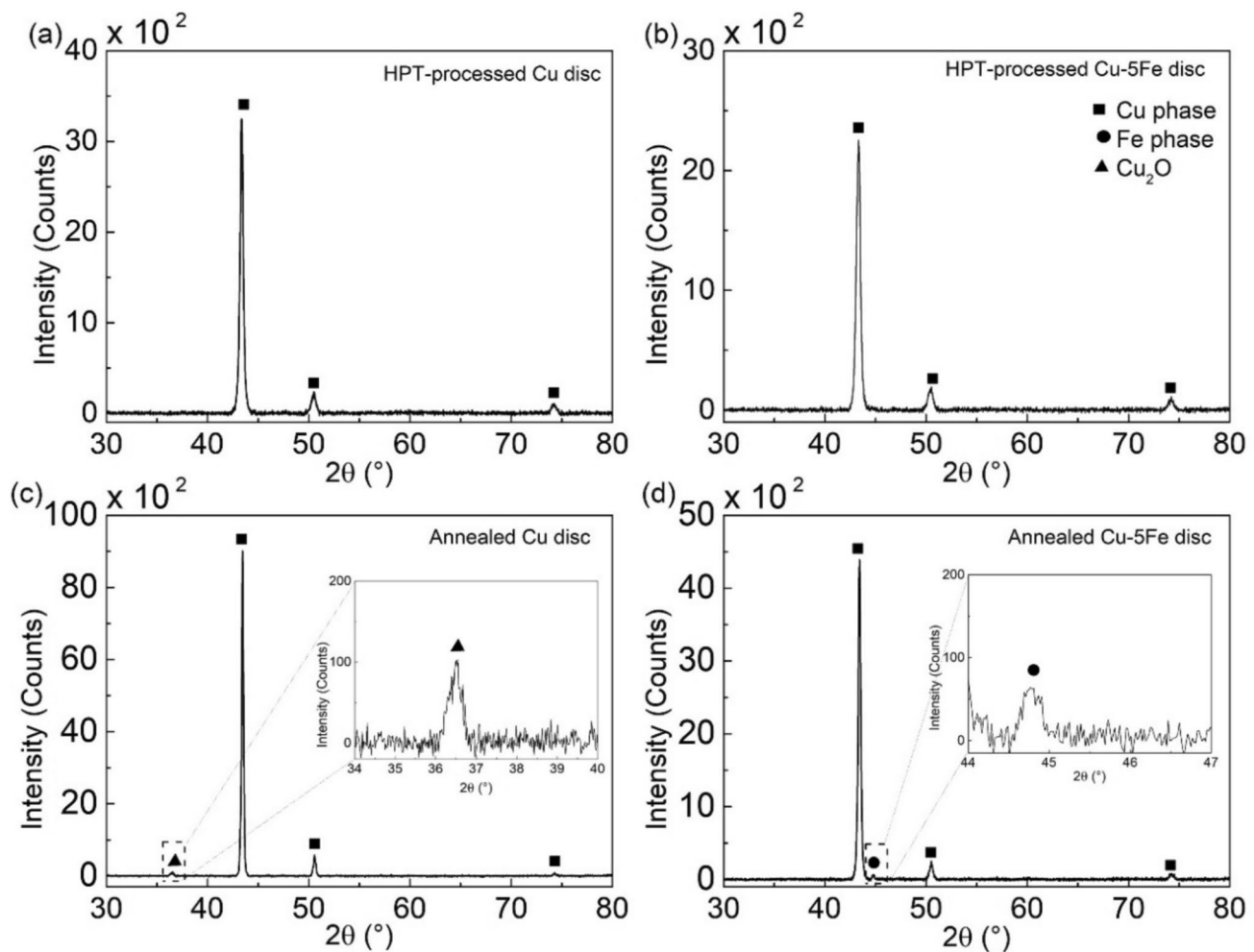


Figure 2 XRD patterns of **a** HPT-processed Cu disc, **b** HPT-processed Cu-5Fe disc, **c** annealed Cu disc and **d** annealed Cu-5Fe disc.

as indicated by the arrows. It was not possible to identify these black spots due to their small size but it may be copper oxide (Cu_2O).

Figure 2c shows that annealing at $500\text{ }^\circ\text{C}$ for 6 h causes the formation of Cu_2O oxide in the annealed Cu disc, as indicated by the development of a peak around $2\theta = 36.5^\circ$. In the case of the annealed Cu-5Fe disc, the XRD pattern in Fig. 2d demonstrates the development of a small peak around $2\theta = 44.7^\circ$ belonging to the Fe phase, thereby confirming a precipitation of the α -Fe phase during the annealing treatment.

EBSD characterization across the disc diameter

The EBSD results revealed the presence of Fe grains in the HPT-processed and annealed Cu-5Fe discs. Thus, for the sake of clarity the microstructural

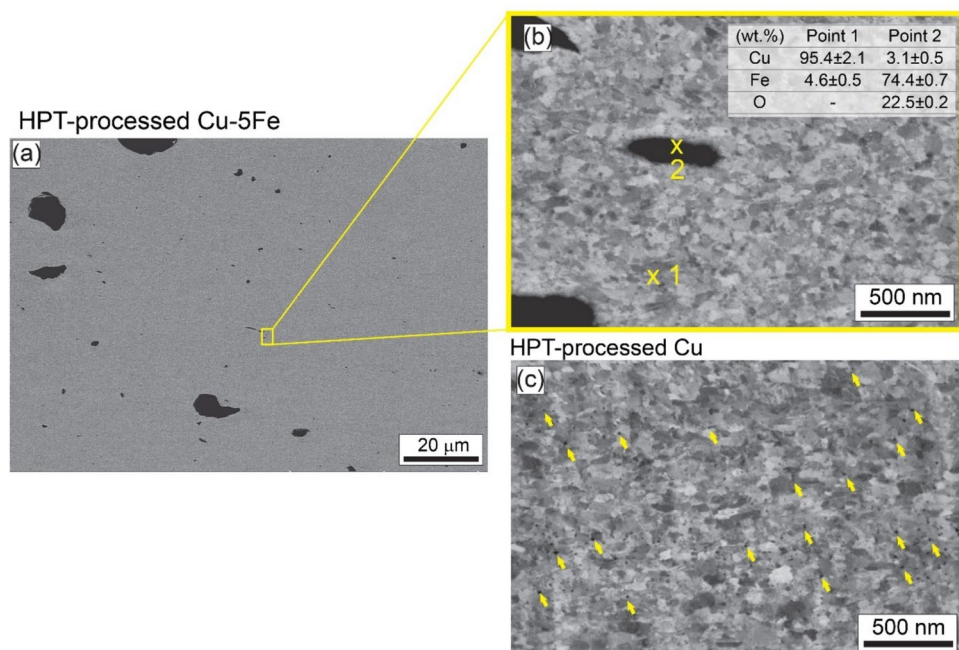
characterizations of the Cu and Fe grains across the disc diameters were separated into two sections.

Microstructure evolution of Cu grains across the disc diameter

The microstructure in the centre, mid-radius and edge on mid-thickness planes of the HPT-processed and annealed Cu and Cu-5Fe discs represented in the form of inverse pole figure (RD-IPF) maps are shown in Figs. 4 and 5, respectively. In the RD-IPF maps, the HAGBs are indicated by black lines. Enlarged zones were inserted in the upper right corner of some RD-IPF maps to easily visualize the Cu grain structure of the samples.

Thus, Fig. 6 displays the evolution of the mean grain size of the Cu grains and HAGBs fraction as a function

Figure 3 SEM photographs with **a** low- and **b** high-magnification showing the microstructure near the mid-radius of the HPT-processed Cu-5Fe disc, EDS analysis at points 1 and 2 present in Fig. 3b and **c** SEM photograph showing the microstructure near the mid-radius of the HPT-processed Cu disc. The arrows in Fig. 3c indicate the presence of small black spots.



of the distance from the centre of the HPT-processed and annealed Cu and Cu-5Fe discs, respectively.

In the case of the HPT-processed Cu disc, the zoomed area at the centre position (Fig. 4a) shows the formation of equiaxed grains with a mean grain size of around 272 ± 30 nm. The grains became elongated along SD (see Fig. 4b and c) and the mean grain size decreased to 224 ± 20 and 200 ± 15 nm (Fig. 6a) at the mid-radius and edge positions, respectively. A net change in grain orientation across the diameter is noticeable. The evolution of texture will be presented in detail later. A microstructure consisting of 76% of HAGBs is obtained at the centre but this is decreased to 62% at the mid-radius and then increased again to 78% at the edge of the HPT-processed Cu disc (Fig. 6b).

Table 1 presents the evolution of dynamic recrystallization (DRX) fraction and the stored energy as a function of distance from the centre of the HPT-processed Cu and Cu-5Fe discs, respectively. It is worth noting that the stored energy has been estimated from GND dislocations and in practice additional stored energies from other lattice defects, such as statistically stored dislocations and vacancies, may be also present in the severely deformed microstructure and contribute to dynamic and static recrystallization [43, 44].

As can be seen, already half of the microstructure at the centre of the HPT-processed Cu disc is

dynamically recrystallized (50.8%). The stored energy at the centre was found to be equal to 35.1 J/mol, but the fraction of DRX decreased (39.1%) and the stored energy increased (43.5 J/mol) at the mid-radius position. At the edge of the HPT-processed Cu disc, the fraction of DRX increases again (64.1%), which causes a decrease in the stored energy to 34.4 J/mol.

In the case of the HPT-processed Cu-5Fe disc, the RD-IPF map of the enlarged area (Fig. 5a) at the centre position shows the development of elongated grains along the SD with a mean Cu grain size equal to 250 ± 25 nm. The grain structure became smaller and equiaxed at the mid-radius (Fig. 5b) and the edge (Fig. 5c) positions and the mean grain size saturated at a value of 190 ± 20 nm (Fig. 6c). A microstructure consisting of 60% of HAGBs is obtained at the centre and the fraction of HAGBs increases slightly to 67% at the edge of the HPT-processed disc (Fig. 6d). It can be observed that the modification in the orientation of grains across the diameter is not drastic by comparison with the HPT-processed Cu disc. Table 1 shows that the fraction of DRX increases gradually from 26.4% at the centre to 31.8 and 33.4% at the mid-radius and edge positions, respectively, whereas the stored energy is found to be similar (~ 44.7 J/mol) at these three positions.

Figure 4d-f shows that a typical recrystallization microstructure of annealed bulk Cu-based alloys is

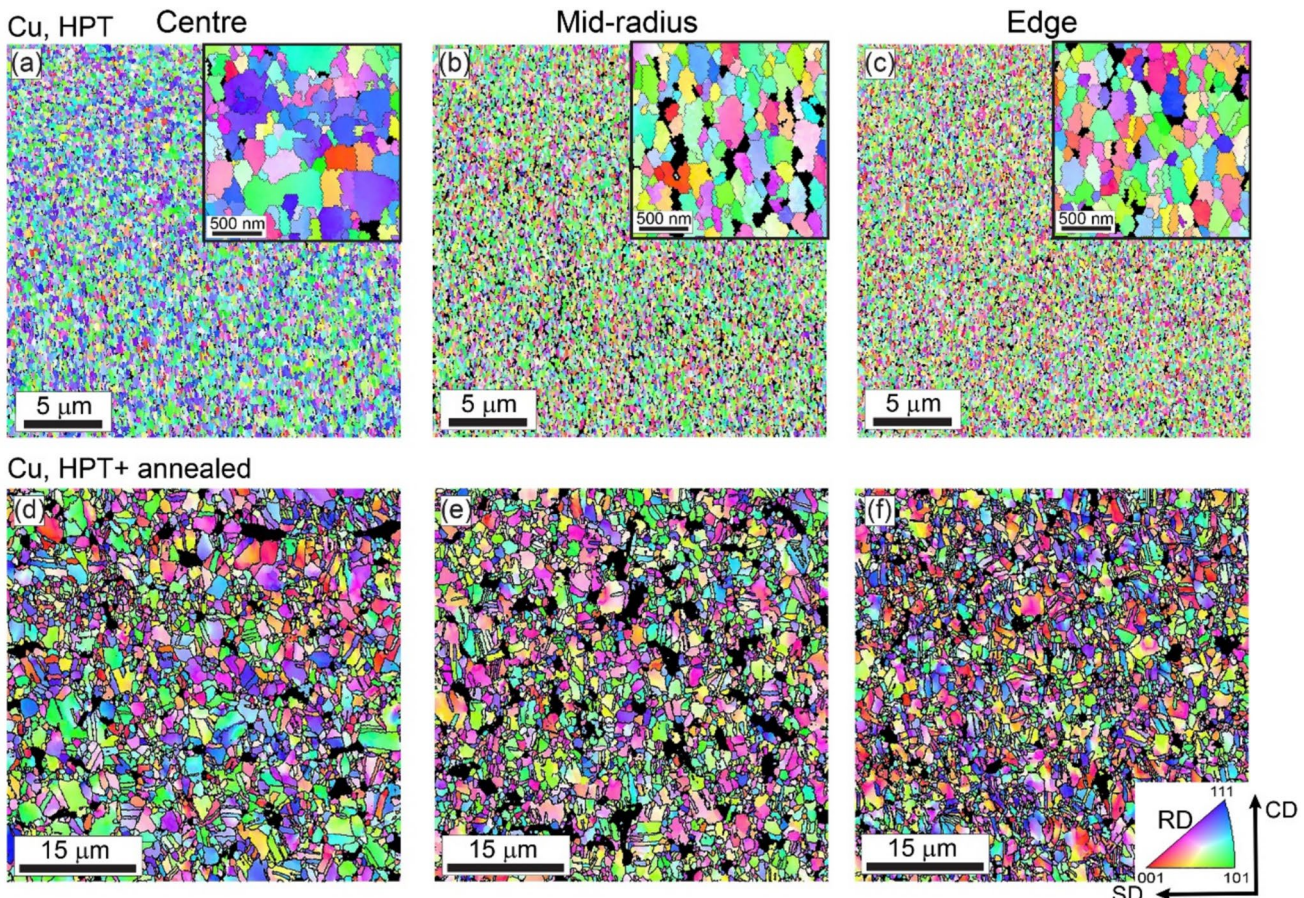


Figure 4 RD-IPF maps at: **a, d** the centre, **b, e** mid-radius and **c, f** edge of HPT-processed and annealed Cu discs, respectively. The color-coded triangle is shown in the bottom right corner of the RD-IPF map (Fig. 4f). The grains in the IPF maps are col-

oured based on their crystallographic directions with respect to RD. Enlarged zones were inserted to visualize the Cu grain structure of the HPT-processed Cu disc (in Fig. 4a-c).

developed in the HPT consolidated Cu disc after the annealing treatment. However, there are many black zones (not indexed areas) which, according to the XRD results (Fig. 2c), could originate from the Cu_2O oxide particles. The coarse grains are decorated with numerous annealing $\Sigma 3$ ($60^\circ < 111 >$) twin boundaries and the estimated fraction of annealing twins was 20, 21 and 15% at the centre, mid-radius and edge of the annealed Cu discs, respectively. According to Fig. 6a, the nanostructure of the HPT-processed Cu disc was lost after annealing in which the mean grain size increased significantly to 2.2 ± 1.1 , 1.9 ± 1.3 and $1.6 \pm 1.5 \mu\text{m}$ at the centre, mid-radius and edge positions, respectively. For additional information, note that the mean grain size was measured by excluding the twin boundaries. In contrast, the HAGBs fraction decreases after the annealing treatment to $\sim 56\%$

at the three positions by comparison with the HPT-processed Cu disc (see Fig. 6b).

The microstructure of the annealed Cu-5Fe disc across the diameter is quite different from the annealed Cu disc. Annealing at 500°C for 6 h of the HPT-processed Cu-5Fe disc leads to the formation of a duplex microstructure formed principally of coarse grains and nano-sized grains at the centre and mid-radius positions of the disc (see Fig. 5d and e). The heterogeneous microstructure is more pronounced at the mid-radius position. Similar to the annealed Cu disc, the larger grains contain several annealing twins and the fraction of twins at the centre and mid-radius was found to be around 6 and 14%, respectively. Consequently, the mean Cu grain size at the centre and mid-radius increases to 380 ± 20 and $750 \pm 25 \text{ nm}$, respectively. In contrast, the microstructure at the edge position of the

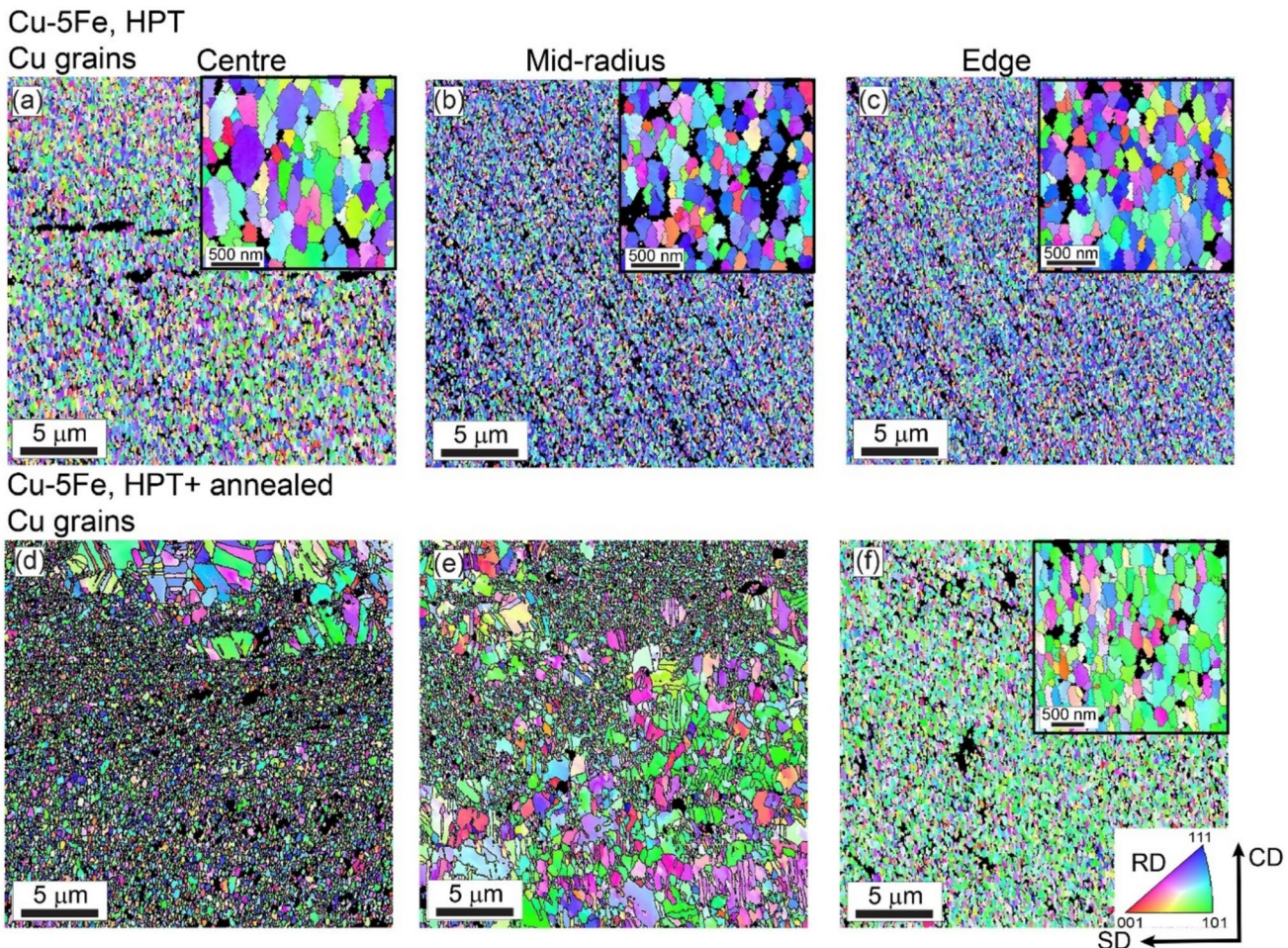


Figure 5 RD-IPF maps showing the Cu grains at: **a**, **d** the centre, **b**, **e** mid-radius and **c**, **f** edge of HPT-processed and annealed Cu-5Fe discs, respectively. The color-coded triangle is shown in the bottom right corner of the RD-IPF map (Fig. 5f). The grains

annealed Cu-5Fe disc remains homogeneously equiaxed nano-sized grains (Fig. 5f) but the mean grain size increases to 250 ± 20 nm (Fig. 6c). The fraction of HAGBs shown in Fig. 6d does not change significantly from the HPT-processed Cu-5Fe disc, except for a slight increase at the centre of the annealed disc (75%). These results originate from the capacity of HPT processing for producing refined microstructures with relatively higher fractions of HAGBs [45].

Microstructure evolution of Fe grains across the disc diameter

Figure 7 presents the RD-IPF maps showing the Fe grains at the centre, mid-radius and edge of the HPT-processed and annealed Cu-5Fe discs, respectively.

in the IPF maps are coloured based on their crystallographic directions with respect to RD. Enlarged zones were inserted to visualize the Cu grain structure of the HPT-processed (in Fig. 5a-c) and annealed Cu-5Fe (in Fig. 5f) discs.

The fraction of Fe grains in each position, estimated based on the OIM software, is displayed in the upper right corner of each RD-IPF map. In contrast to the XRD results (Fig. 2b), the EBSD measurements revealed the presence of the Fe phase, as in Fe grains, in the HPT-processed Cu-5Fe disc. According to the OIM software, the Fe phase fraction estimated at the centre was relatively weak, about 3% and it seems to decrease to 1.7% and 1.3% at the mid-radius and the edge of the disc, respectively. This could explain why the Fe phase was not detected by XRD analysis. Furthermore, the shape and the distribution of the Fe phase are also affected by the measurement position. It can be observed that the Fe phase at the centre of the disc (Fig. 7a) is in the form of a band parallel to SD and then becomes smaller and uniformly distributed

Figure 6 Evolution of mean grain size and HAGBs fraction at the centre, mid-radius and edge of the HPT-processed and annealed: **a**, **b** Cu and **c**, **d** Cu-5Fe discs, respectively.

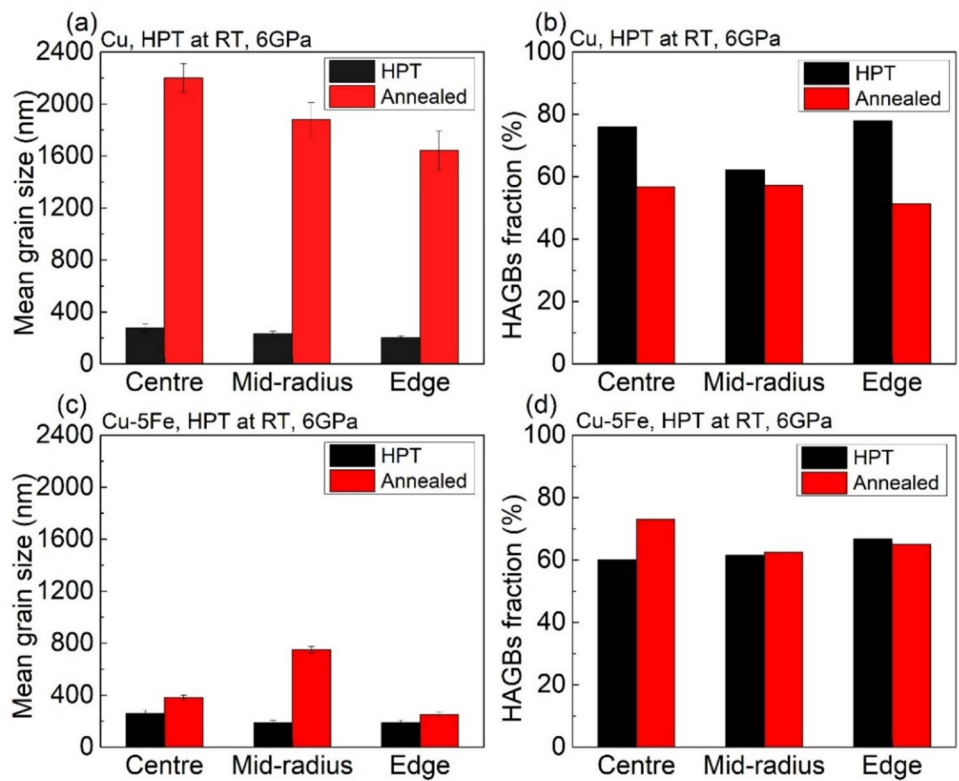


Table 1 Fraction of DRX and stored energy at the centre, mid-radius and edge of the HPT-processed Cu and Cu-5Fe discs

	HPT-processed Cu		HPT-processed Cu-5Fe	
	DRX (%)	E_s (J/mol)	DRX (%)	E_s (J/mol)
Centre	50.8	35.1	26.4	44.4
Mid-radius	39.1	43.5	31.8	44.7
Edge	64.1	34.4	33.4	44.7

towards the edge of the HPT-processed Cu-5Fe disc (Fig. 7b and c).

The mean grain sizes of the Fe grains in the HPT-processed and annealed Cu-5Fe discs are summarized in Table 2. It is worth noting that further microstructural features for the Fe grains, such as the HAGBs fraction, were not evaluated because of their low values and their arbitrary distribution in the EBSD maps.

Table 2 indicates that the Fe grains at the centre position exhibits a value of 250 ± 15 nm and it decreases continuously with increasing the distance from the centre of the disc to reach a value of 125 ± 10 nm at the edge position.

Figure 7d-f revealed that the fraction of the Fe phase increases with respect to the deformation state

to 7.0, 4.3 and 4.0% at the centre, mid-radius and edge of the annealed Cu-5Fe disc, respectively, and their size becomes larger after annealing as is evident by Table 2. The mean grain size of the Fe grains increases to 270 ± 20 , 220 ± 15 and 170 ± 20 nm at the centre, mid-radius and edge of the annealed Cu-5Fe disc, respectively.

STEM characterization

Figure 8 presents additional microstructural observations taken near the mid-radius of the HPT-processed Cu and Cu-5Fe discs using STEM in BF and HAADF modes with different magnifications. The STEM photographs in BF of the HPT-processed Cu (Fig. 8a) and Cu-5Fe (Fig. 8d) discs revealed the development of nanocrystalline grain structures which were relatively homogeneously distributed through the microstructures. The STEM images in the HAADF mode provide evidence of nano-sized particles with a circular shape of copper oxide (blue arrows) in the HPT-processed Cu disc (Fig. 8b) and iron oxide (red arrows) in the HPT-processed Cu-5Fe disc (Fig. 8e). In Fig. 8c, a stacking fault (green arrow) and nano-sized lamella deformation twins (yellow arrows) are visible in the

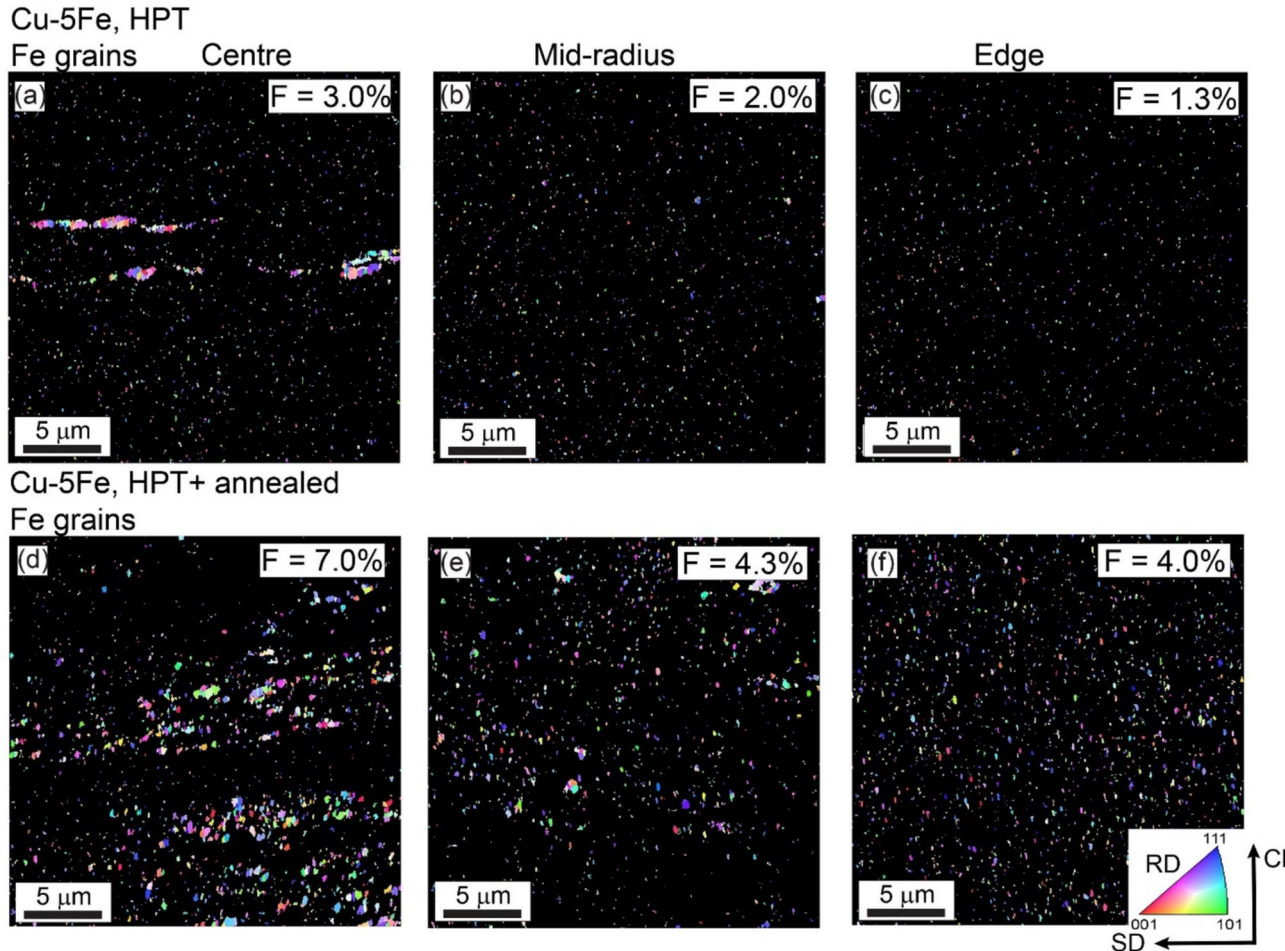


Figure 7 RD-IPF maps showing the Fe grains at: **a, d** the centre, **b, e** mid-radius and **c, f** edge of HPT-processed and annealed Cu-5Fe discs, respectively. The color-coded triangle is shown in the bottom right corner of the RD-IPF map (Fig. 7f). The grains in

the IPF maps are coloured based on their crystallographic directions with respect to RD. The fraction of Fe grains is indicated in the upper right corner of the RD-IPF maps.

HPT-processed Cu disc. The HPT-processed Cu-5Fe disc also revealed the presence of nano-sized twins as indicated by the yellow arrow in Fig. 8d.

Figure 9 depicts the STEM images in BF and HAADF modes with the corresponding EDS mapping for the Cu, Fe and O elements for the annealed Cu-5Fe disc, respectively. Similar to the EBSD results

(Fig. 5e), the STEM image shows the development of a duplex microstructure after the annealing treatment. Annealing twins are easily recognized, as indicated by the yellow arrow in Fig. 9a. Interesting findings can be seen from the STEM and EDS mapping in which the small refined grains are surrounded by large (~160 nm) and nano-sized (~70 nm) iron oxide Fe_2O_3 particles while the coarse grains are completely free from Fe and O elements. A close inspection of Fig. 9d reveals the homogenous distribution of the Fe element in the region with small grains which means that the nano-sized grains achieve a uniform solid solution state.

Table 2 Evolution of mean grain size of Fe grains as a function of distance from the centre of HPT-processed and annealed Cu-5Fe discs

Grain size of Fe grains (nm)	Centre	Mid-radius	Edge
HPT-processed Cu-5Fe	250 ± 15	139 ± 10	125 ± 10
Annealed Cu-5Fe	270 ± 20	220 ± 15	170 ± 20

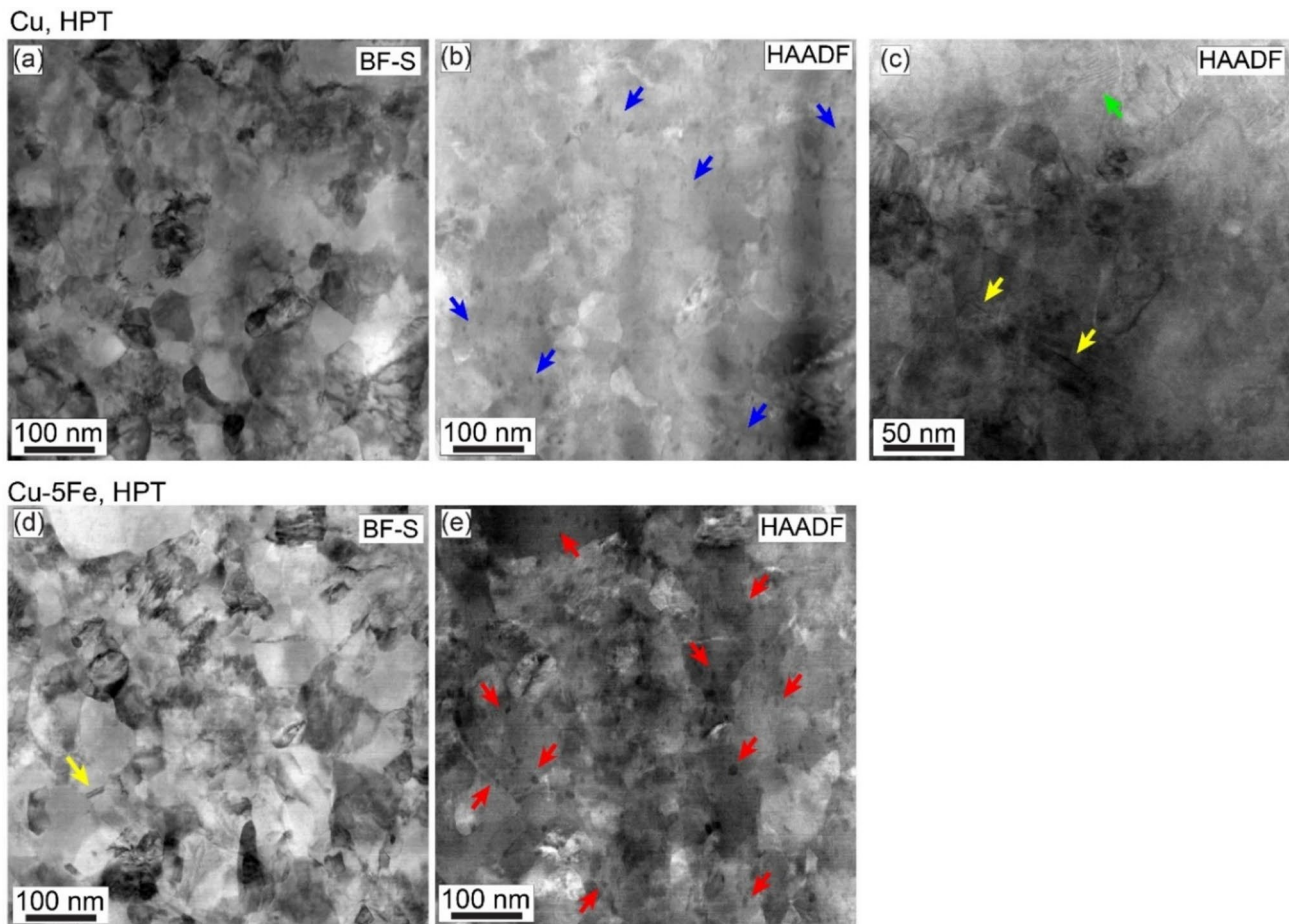


Figure 8 STEM images in BF and HAADF modes for the HPT-processed: **a-c** Cu and **d, e** Cu-5Fe discs, respectively.

Texture evolution across the disc diameter

Texture evolution of Cu grains across the disc diameter

Figures 10 and 11 present the ODF sections at $\varphi_2 = 0$ and 45° at the centre, mid-radius and edge of the HPT-processed and annealed Cu and Cu-5Fe discs, respectively. It must be noted that the ODF sections presented in Fig. 11 show the texture of Cu grains in the HPT-processed and annealed Cu-5Fe discs. The positions of the ideal shear texture components for FCC materials are indicated in the ODF sections and their description in Miller indices ($\{hkl\} <uvw>$) and Euler angles ($\varphi_1, \Phi, \varphi_2$) are summarized in Table 3 [46]. Basically, HPT processing led to the formation of a simple shear texture type characterized by the formation of two fibres [46]. Thus, the *A*-fibre ($\{111\} // \text{RD-SD plane}$) contained the A, \bar{A}, A_1^* and A_2^* components [46] and the second fibre named *B*-fibre

($\{<110>\} // \text{SD}$) contained the A, \bar{A}, B, \bar{B} , and *C* components [46].

At the centre of the HPT-processed Cu disc (Fig. 10a), the texture exhibits the formation of partial *B*-fibre (presence of B/\bar{B} , and A/\bar{A} components and absence of *C* component) and partial *A*-fibre (presence of $A/\bar{A}, A_1^*$ components and absence of A_2^* component) with a strong A_1^* component (6.5 mrd, multiple random distribution). The texture components belonging to the *A*-fibre and *B*-fibre are located in their ideal positions. The texture completely changes at the mid-radius position (see Fig. 10c), where *B* and \bar{B} disappeared and the *A* and A_2^* components appeared with an obvious deviation from their ideal positions and the spread of the A_2^* orientation. Thus, the partial *B*-fibre vanished, while the partial *A*-fibre persists but with the presence of *A* and A_1^*/A_2^* components and the absence of the \bar{A} component.

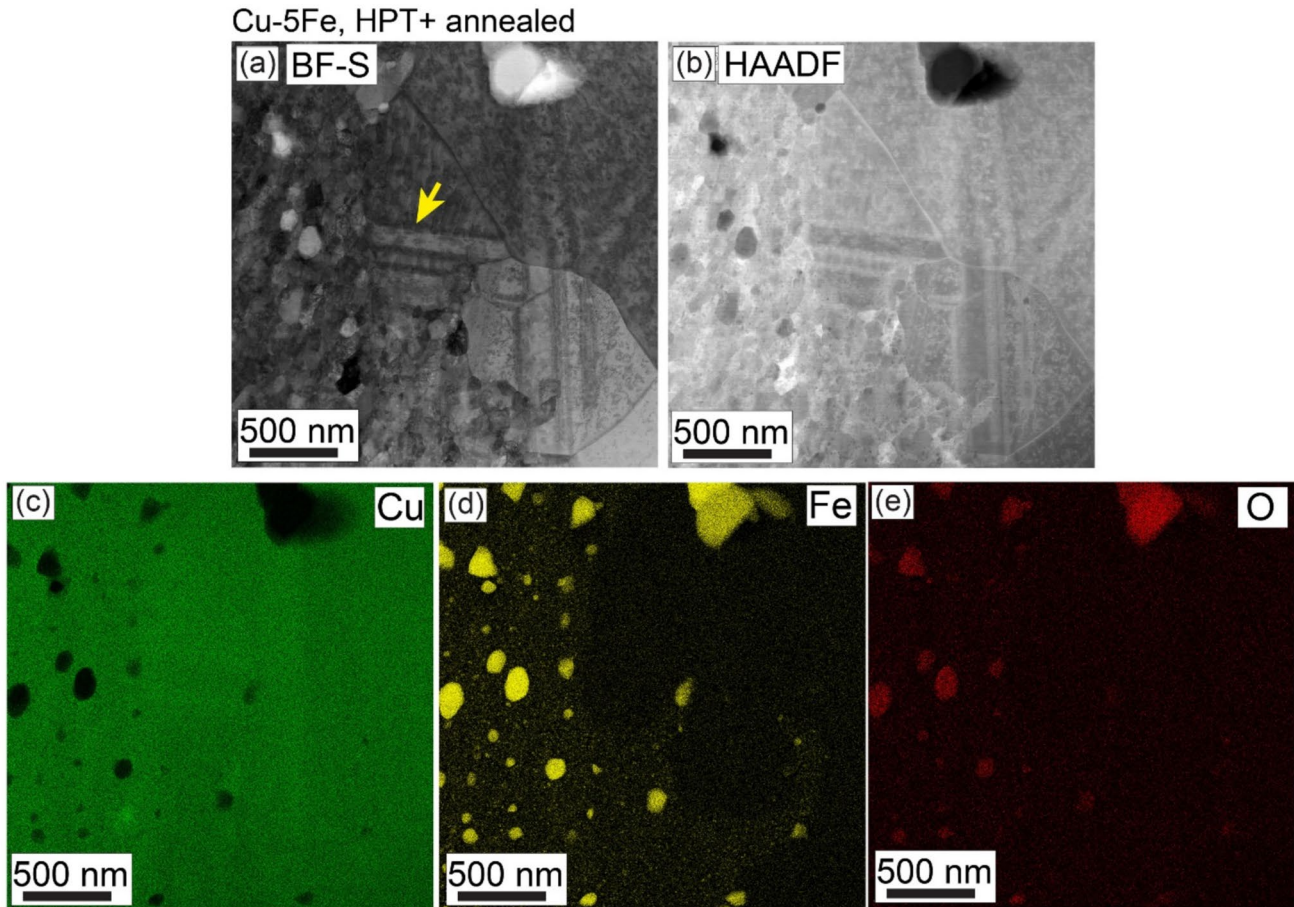


Figure 9 STEM image in **a** BF and **b** HAADF modes with the corresponding EDS mapping for **c** Cu, **d** Fe and **e** O elements for the annealed Cu-5Fe disc, respectively.

Figure 10e shows that the texture at the edge of the HPT-processed Cu disc is very similar to that at the mid-radius position.

Annealing at 500 °C for 6 h maintained the deformation texture reasonably across the distance from the centre of the Cu disc. As can be seen from Fig. 10b, the A_2^* component appeared and the intensity of the partial B -fibre decreased at the centre of the annealed Cu disc. The deformation texture was principally retained at the mid-radius position (Fig. 10d) but with strengthening of the A component (7.3 mrd). The texture at the edge of the annealed Cu disc (Fig. 10f) was retained and tends to be weaker with respect to the texture of the HPT-processed Cu disc.

For the HPT-processed Cu-5Fe disc, the ODF sections at the centre of the disc, shown in Fig. 11a, indicated the presence of the A_2^* component with the gradual formation of partial B -fibre due to the presence of the C and B components but with a visible

deviation from their ideal positions. Figures 11c and e revealed that the textures at the mid-radius and edge positions are identical, where the C component disappeared and a net strengthening of the A_2^* and B components is noted. In both mid-radius and edge positions, a maximum texture intensity of 8.7 mrd is located between the A_2^* and B components at (220°, 65°, 45°), as indicated by the arrow in the ODF section at $\varphi_2 = 45^\circ$ (Fig. 11c and e).

The texture at the centre of the annealed Cu-5Fe disc is different from the deformed texture at the same position, where the C component was replaced by A_1^* and A components leading to the formation of the partial A -fibre (presence of A_1^*/A_2^* and A components and absence of \bar{A} component). It can be observed that the B component remains present and the shear texture components are more located at their ideal positions (see Fig. 11b). From Fig. 11d and

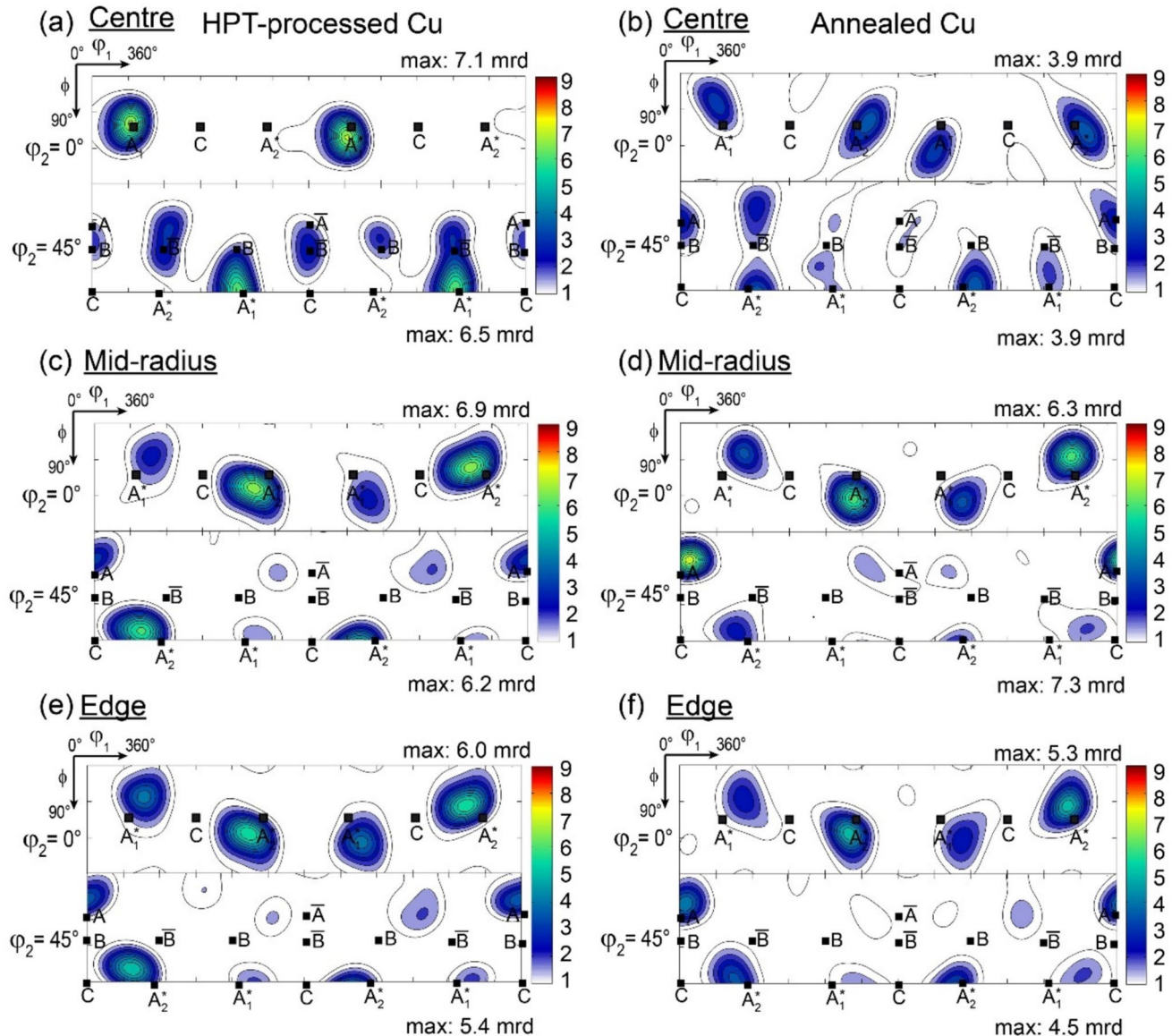


Figure 10 ODF sections at $\varphi_2=0$ and 45° at: **a, b** the centre, **c, d** mid-radius and **e, f** edge of HPT-processed and annealed Cu discs, respectively. The positions of the ideal shear texture components are indicated in the ODF sections.

f, it is evident that the textures at the mid-radius and edge positions were significantly changed after the annealing treatment. The B component disappeared, and it was replaced by a scattered A_2^* component, \bar{A} and weak C and deviated A_1^* components. A complete A-fibre (presence of A/\bar{A} and A_1^*/A_2^* components) tends to form at the mid-radius position. The texture at the edge of the Cu-5Fe disc is quite similar to the mid-radius position, except for the absence of C component and strengthening of A_1^* component.

Consequently, a full A-fibre is formed with the dominance of the A_2^* component.

Texture evolution of Fe grains

For statistical purposes, the texture of the Fe phase in the deformation and annealing conditions was analysed only at the centre position (highest Fe fraction) and the results are presented in Fig. 12 in terms of ODF sections at $\varphi_2=0$ and 45° . The positions of the

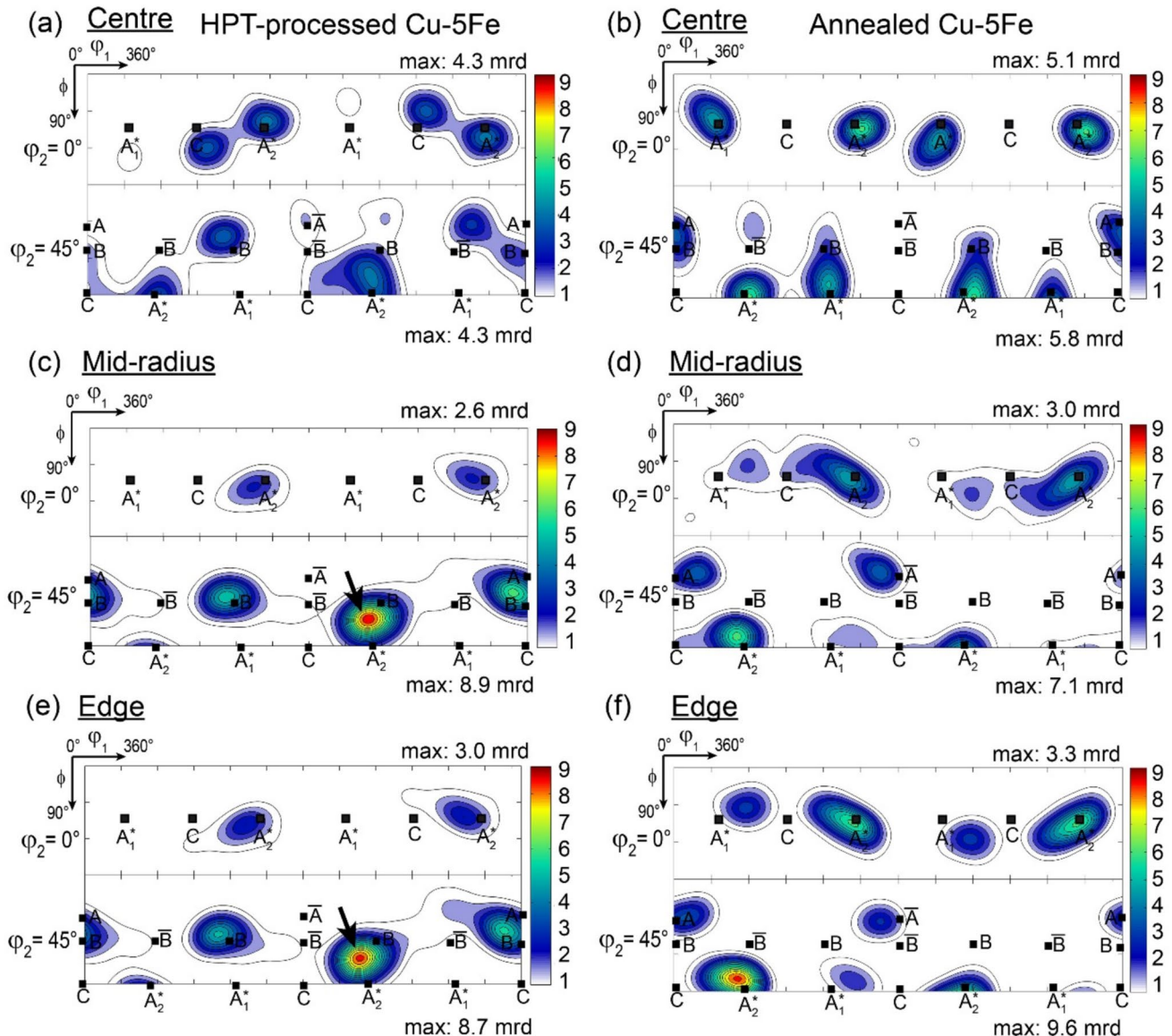


Figure 11 ODF sections at $\varphi_2=0$ and 45° showing the texture of the Cu grains at: **a, b** the centre, **c, d** mid-radius and **e, f** edge of HPT-processed and annealed Cu-5Fe discs, respectively. The

positions of the ideal shear texture components are indicated in the ODF sections.

ideal shear texture components for BCC materials are indicated in the ODF sections and their description in Miller indices ($\{hkl\} <uvw>$) and Euler angles ($\varphi_1, \Phi, \varphi_2$) are summarized in Table 3 [46].

The ODF sections in Fig. 12a indicate the gradual formation of the typical shear texture of BCC materials with the formation of near F , J and \bar{J} components. D_1 and D_2 components were also developed but with an obvious deviation from their ideal positions. Annealing at 500°C for 6 h led to the formation of a typical shear texture where all shear components were present

in their ideal positions and with a visible strengthening around the J and \bar{J} components (see Fig. 12b).

Mechanical properties

Figure 13 displays two-dimensional microhardness maps over the vertical cross sections along the diameters of the HPT-processed and annealed Cu and Cu-5Fe discs, respectively. Before HPT processing, the compacted Cu and Cu-5Fe discs exhibited average Vickers microhardness values of ~ 47.4 and ~ 48.8 Hv,

Table 3 Ideal position of shear texture components for FCC and BCC materials projected in the SD-CD plane [46]

Shear texture for FCC materials			Shear texture for BCC materials		
Notation	Miller indices $\{hkl\} <uvw>$	Euler angles ($^\circ$) ($\varphi_1, \Phi, \varphi_2$)	Notation	Miller indices $\{hkl\} <uvw>$	Euler angles ($^\circ$) ($\varphi_1, \Phi, \varphi_2$)
<i>A</i>	$\{112\} <1\bar{1}0>$	(0, 35.2, 45)	<i>D</i> ₁	$\{011\} <1\bar{1}1>$	(54.7, 45, 0)
\bar{A}	$\{211\} <0\bar{1}1>$	(50.7, 65.9, 63.4)	<i>D</i> ₂	$\{011\} <\bar{1}11>$	(125.2, 45, 90)
<i>A</i> ₁ [*]	$\{101\} <\bar{1}21>$	(35.26, 45, 90)	<i>J</i>	$\{111\} <\bar{1}\bar{1}2>$	(90, 54.7, 45)
<i>A</i> ₂ [*]	$\{011\} <\bar{2}11>$	(144.7, 45, 0)	\bar{J}	$\{111\} <1\bar{2}1>$	(30, 54.7, 45)
<i>B</i>	$\{111\} <1\bar{1}0>$	(0, 57.4, 45)	<i>E</i>	$\{112\} <\bar{1}\bar{1}1>$	(90, 35.2, 45)
\bar{B}	$\{111\} <0\bar{1}1>$	(60, 54.7, 45)	\bar{E}	$\{112\} <11\bar{1}>$	(270, 35.2, 45)
<i>C</i>	$\{110\} <1\bar{1}0>$	(0, 90, 45)	<i>F</i>	$\{011\} <100>$	(0, 45, 0)

$\{hkl\} // SD-CD$ plane, $<uvw> // CD$

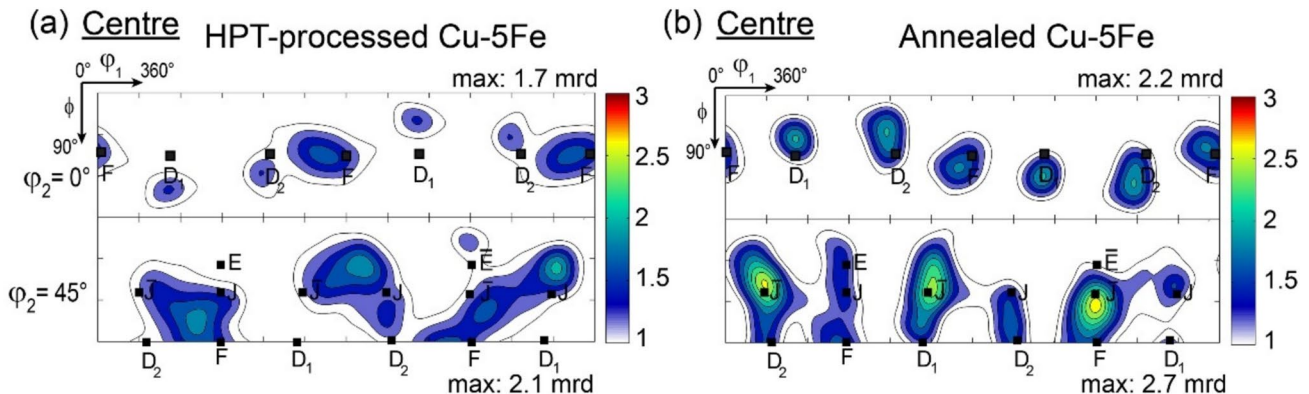


Figure 12 ODF sections at $\varphi_2=0$ and 45° showing the texture of Fe grains at the centre of: **a** HPT-processed and **b** annealed Cu-5Fe discs. The positions of the ideal shear texture components for BCC materials are indicated in the ODF sections.

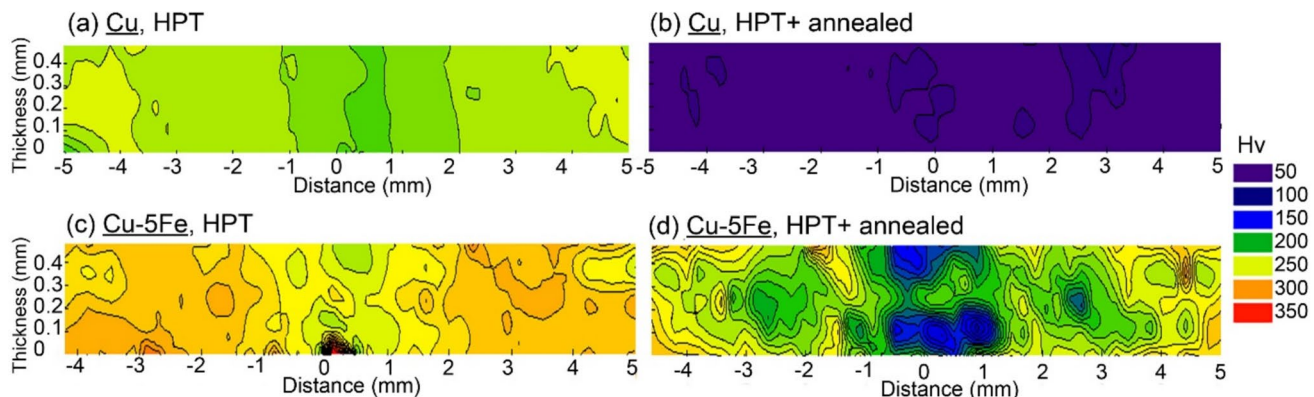


Figure 13 Hv mapping of HPT-processed and annealed: **a, b** Cu and **c, d** Cu-5Fe discs, respectively.

respectively. For both HPT-processed discs (Fig. 13a and c), the microhardness increases with increasing distance from the centre of the disc. For example, in the middle section, the microhardness at the centre of the HPT-processed Cu disc was found equal to 217 Hv

and it increases to 233 and 238 Hv at the mid-radius and edge positions, respectively. For the HPT-processed Cu-5Fe disc, a value of 237 Hv was recorded at the centre position and it increases to 275 Hv at the mid-radius and then reaches a steady state after that

(276 Hv at the edge position). Thus, it is evident that the Cu-5Fe disc is harder than the Cu disc.

The microhardness decreased after annealing treatment at 500 °C for 6 h (see Fig. 13b) and becomes homogeneously distributed across the Cu disc where an average value of 45 Hv is reached. While annealing at 500 °C for 6 h led to a softening in which the decrease in the microhardness is extended from the centre to the edge of the annealed Cu-5Fe disc (Fig. 13d). For example, the value of microhardness at the centre, mid-radius and edge positions were about 135, 233 and 265 Hv, respectively. It is interesting to note that the decrease in the microhardness at the edge is small with respect to the deformed state at the same position (276 Hv).

Based on the microhardness values, the deformation inhomogeneity can be accessed through the inhomogeneity factor, *IF*, using the following equation [47, 48]:

$$IF = \frac{\sqrt{\sum_{i=1}^n (Hv_i - Hv_{ave})^2 / n - 1}}{Hv_{ave}} \times 100 \quad (2)$$

where *n* is the number of microhardness measurements on each sample, Hv_{ave} is the average microhardness value, and Hv_i is the microhardness value of the *i*th measurement. Basically, a low *IF* value reflects a regular distribution of mechanical properties across the microstructure [48].

The values of *IF* for the HPT-processed and annealed Cu and Cu-5Fe discs are presented in Table 4. As can be noted, the HPT-processed Cu exhibits the lowest *IF* value (3.1%) and it increases significantly after annealing treatment (*IF* = 13.9%). For the Cu-5Fe disc, the highest value is recorded under HPT processing (*IF* = 20.7%) and then it decreases to 14.7% after the annealing treatment.

Nevertheless, the observed hardness variations across the thickness of the HPT disc, which are especially pronounced after annealing, are attributed to the distinct shear patterns developed during HPT

processing [49]. A greater shear strain near the disc surface promotes the earlier microstructural relaxation and this behaviour is supported by recent studies: TEM analysis of HPT-processed Al-Mg alloys revealed enhanced solid-state mixing near the disc surfaces [50]. Furthermore, XRD analysis showed an accelerated phase transformation near the disc surfaces which was more than the mid-thickness of nanostructured TiAl intermetallics [51], and in situ high-temperature laser-scanning confocal microscopy showed accelerated recovery at the surfaces of HPT-processed CoCrHeNiMn alloys [52].

Discussion

Deformation behaviour and texture evolution of consolidated discs

The experimental results concerning the deformation microstructures of the Cu and Cu-5Fe discs demonstrated that HPT processing at RT through 30 turns under an applied pressure of 6 GPa was effective for consolidation and mixing the immiscible Cu and Fe elements and provides the capability to form a bulk material with a nanocrystalline grain structure (Figs. 4 and 5), a relatively large number of HAGBs (Fig. 6b and d) and a shear-type texture (Figs. 10 and 11). In addition, during the consolidation, CuO₂ oxide particles formed in the pure Cu disc and Fe grains and Fe₂O₃ oxide particles formed in the Cu-5Fe disc (see Fig. 8). For both materials, the microstructural features, texture and microhardness evolution (Fig. 13a and c) were dependent upon the distance from the centre of the disc. This is reasonable since the equivalent strain, ε_{eq} , increases with increasing radial distance from the centre of the HPT-processed disc, as indicated by the following equation [53]:

$$\varepsilon_{eq} = \frac{2\pi Nr}{\sqrt{3}h} \quad (3)$$

where *N* is the number of HPT turns, *r* is the radial distance from the centre of the disc and *h* is the thickness of the disc. Accordingly, the equivalent strains calculated at the centre, mid-radius and edge positions were 36.2, 453.2 and 815.7, respectively.

In the majority of conventional bulk materials with medium to high stacking fault energies, such as Cu (~78 mJ/m²) and Al (~160 mJ/m²), the mean grain

Table 4 *IF* values for the HPT-processed and annealed Cu and Cu-5Fe discs

	HPT-processed Cu	Annealed Cu	HPT-processed Cu-5Fe	Annealed Cu-5Fe
<i>IF</i> (%)	3.1	13.9	20.7	14.7

size decreased and the microhardness increased with increasing distance from the centre of the disc at low numbers of HPT turns due to the increase in shear strain (Eq. 3) and often a steady state across the disc is reached rapidly after 5 HPT turns which corresponds to the strain range of $\varepsilon_{\text{eq}} \sim 6\text{--}150$ [22, 46, 54]. Regarding the texture, the development of a shear texture is unstable and gradually formed at low strain and then often stabilizes at the same strain level as the grain refinement [46]. Generally, the grain refinement during the HPT processing can be divided into the two stages of grain fragmentation and saturation [55]. In these materials, the deformation is accommodated by the activation of dislocation slip systems, their accumulation to form dislocation cell structure and then their gradual transformation into HAGBs with increasing shear strain to form new ultrafine or nanosized grains through a continuous dynamic recrystallization (CDRX) mechanism [56]. A discontinuous dynamic recrystallization (DDRX) mechanism, which is characterized by the formation of recrystallized grains along the grain boundaries through nucleation and a growth process [56], can occur concurrently with CDRX during the fragmentation stage [57].

According to these results, a homogeneity in grain refinement and microhardness evolution across the disc diameter in both consolidated Cu and Cu-5Fe discs was not reached even after 30 HPT turns ($\varepsilon_{\text{eq}} \approx 36.2\text{--}815.7$) and may require more HPT turns. Indeed, it was recently reported that HPT processing for 100 turns with an applied strain around ~ 3000 was required for obtaining a steady-state in the consolidated Cu-14Fe (wt.%) disc [31]. Thus, it is harder to achieve a complete saturation in the microstructure and microhardness in the consolidated powders than in conventional FCC bulk materials. In addition, the present results indicated that the deformation characteristics of the Cu and Cu-5Fe discs were different.

It is clear from the experimental data that the grain refinement and mechanical properties of the HPT-processed Cu disc failed to reach a steady-state condition across the disc diameter although the texture was stable at the mid-radius and edge of the disc. In contrast, the HPT-processed Cu-5Fe disc appears to follow the deformation behaviour of HPT-processed bulk materials, where the mean grain size decreases and the microhardness increases from the centre to the mid-radius and saturates thereafter ($\varepsilon_{\text{eq}} = 453.2$). In addition, the texture was stable starting from the mid-radius of the disc.

In contrast to the HPT processing of bulk material, the shear deformation during HPT processing of powder particles plays two major roles [58–60]. At first, the continued shear deformation assures particle bonding and reduces the porosity. It is assumed that the substantial reduction in the particle size, high vacancy concentration and capillary pressures are the thermodynamic driving forces allowing the mechanical alloying of the Fe and Cu elements [27, 61]. Second, when the particle bonding is achieved, grain refinement is produced with further shear deformation. Thus, the microstructure and texture evolutions are expected to be different and more complicated than in the case of conventional bulk processed materials.

The results concerning the HPT-processed Cu disc indicate the development of high fractions of HAGBs (76%) and DRX (50.8%) at the centre position which mean the production of rapid grain refinement. This is supported by the formation of well-defined partial *B*-fibre and *A*-fibre textures. The drop in the fraction of HAGBs (62.2%) and DRX (39.1%) at the mid-radius position is explained by the occurrence of grain fragmentation. For a more detailed analysis, Fig. 14 shows the enlarged zones of the microstructure at the centre, mid-radius and edge of the HPT-processed Cu disc already presented in Fig. 4 superposed with sub-grain boundaries, LAGBs and HAGBs in red, green and black colours.

As already noted, the microstructure at the centre of the disc contains a relatively low fraction of sub-grain boundaries and a very high fraction of HAGBs indicating the development of ultrafine grains through the DRX process. A high fraction of sub-grain boundaries (30.6%) is noticed in the mid-radius indicating a generation of new dislocations and this explains the increase in the stored energy (43.5 vs. 35.1 J/mol at the centre position). At this stage, the increase of dislocation density originates from the change in texture at the mid-radius position (see Fig. 10c) which allows the activation of additional dislocation slip systems and their accumulation to form sub-grain boundaries. The change and the oscillation in the texture is mainly attributed to the amount of shear deformation and the heterogenous shear strain distribution due to the continuous rotation of the sample disc during the HPT processing [46, 62]. Based on Eq. 3, the equivalent strain at the centre position was low ($\varepsilon_{\text{eq}} = 32.2$) and it increases significantly at the mid-radius to $\varepsilon_{\text{eq}} = 453.2$ and at the edge to $\varepsilon_{\text{eq}} = 815.7$. This is supported by the

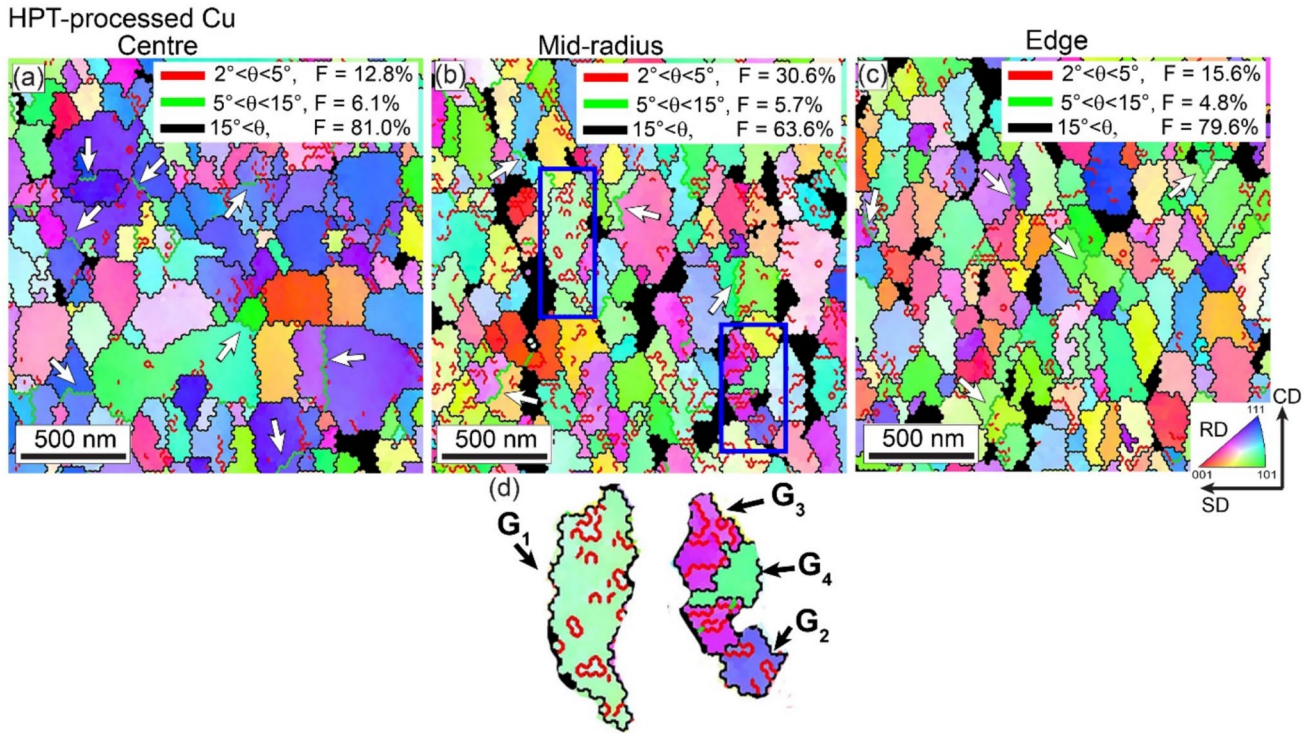


Figure 14 RD-IPF enlarged maps from Fig. 4 superposed with grain boundary type at: **a** the centre, **b** mid-radius and **c** edge of the HPT-processed Cu disc, respectively. **d** G_1 , G_2 , G_3 and G_4 are

similar texture modification in the HPT-processed Cu-5Fe disc at the same strain level (Fig. 11c).

In the blue boxes shown in Fig. 14b there are some examples about the distribution of sub-grain boundaries within the grains. As shown in the elongated grain (G_1), the sub-grain boundaries are located inside the grains which increase the intragranular orientation spread and near the grain boundaries indicate the simultaneous triggering of the CDRX and DDRX mechanisms.

In the equiaxed blue grain (G_2), the sub-grain boundaries are only located near the grain boundaries showing the dominance of the DDRX mechanism. By contrast, in the purple grain (G_3) the distribution of sub-grains inside the grains is in the form of a straight line giving a typical fragmentation structure. By contrast, the green grain (G_4) is free from dislocations. These observations confirm the dependency of grain fragmentation on both grain orientation and grain size. Thus, not all grains go through the same level of plastic deformation at the same time and this may be another element influencing the texture modification over the disc diameter.

examples to illustrate the dependency of sub-grains boundaries on the grain orientation.

The EBSD analysis shows that dislocations are the main deformation mode to accommodate the deformation under HPT processing. However, STEM observations (Fig. 8) indicate the presence of deformed nano-twins in both the HPT-processed Cu and Cu-5Fe discs. It was found that the nanocrystalline copper promotes the formation of deformation twins during HPT processing at RT [63] and this was attributed to a partial dislocation emission from the grain boundaries [63]. It is well known that deformation twining is responsible for a texture transition during rolling of FCC materials with low stacking fault energy [64]. In the present study however, it is not possible to reach conclusions on the role of deformation nano-twins in the texture modification at the mid-radius and edge of the discs.

At the edge of the disc (see Fig. 14c), the sub-grain boundaries decreased (15.6%) due to their continuous accumulation and their transformation into HAGBs (79.6%) thereby creating new nano-sized grains with a mean size (200 ± 15 nm) smaller than at the centre (275 ± 30 nm) of the disc. This is corroborated by the increase in the DRX fraction and the decrease in the stored energy as shown in Table 1. It is interesting to

note that the fraction of LAGBs varied very little across the disc diameter (6.1, 5.7, 4.8% at the centre, mid-radius and edge positions, respectively). It is evident from the maps that the remaining LAGBs are mainly grain boundaries between grain neighbourhoods with similar orientations, as designated by white arrows in the three RD-IPF maps (Fig. 14). Based on the latter observation, it is proposed that the consolidation of pure Cu powder by HPT processing through 30 turns undergoes two grain refinement stages. Thus, at the centre of the disc which corresponds to an equivalent strain of 36.2, the material already reached the saturation stage of the first grain refinement process. At the mid-radius where $\epsilon_{eq} = 453.2$, the material is in the fragmentation stage of the second grain refinement process. Finally, at the edge of the disc ($\epsilon_{eq} = 815.7$), the material reached the saturation stage of the second grain refinement process. It should be noted that the production of two grain refinement stages accompanied by two hardening stages was also reported in HPT-processed aluminium-based alloys [57, 65].

During the second grain refinement regime, a partial *A*-fibre with a dominance of the A_2^* component developed (see Fig. 10c and e) during the grain fragmentation and saturation stages. The development of an *A*-fibre texture was reported earlier in Cu-based alloys processed by HPT processing such as pure Cu [66], Cu/Ni layers [67] and a Cu-Ni-Si alloy [68].

Regarding the HPT-processed Cu-5Fe disc, the low DRX fraction and the high stored energy indicates that grain refinement rate was slower than for the HPT-processed Cu disc (see Table 1). Also, the development of a typical shear texture was restricted as is evident from the texture evolution at the centre of the HPT-processed disc (see Fig. 11a). Moreover, the saturation in the stored energy (44.7 J/mol) across the HPT-processed Cu-5Fe disc diameter suggests a balance between the generation and annihilation of dislocations where this evolution is a consequence of the addition of the Fe element which plays a major role as a solid solution element preventing dislocation movement and hence slowing the occurrence of the DRX process. This is supported by noting that the fraction of Fe grains (Fig. 7) and their corresponding grain size (Table 2) decreased at the mid-radius and edge positions which means that the Fe grains were sheared and fragmented under the HPT processing and the Fe element dissolved in the Cu matrix.

In addition, due to the difference in the intrinsic characteristics of the Cu and Fe grains, the creation of

phase boundaries may play an important role in preventing dislocation movement and thereby inhibiting the DRX process and increasing the stored energy. The presence of Fe_2O_3 oxide particles as shown in the SEM (Fig. 3) and STEM observations (Fig. 8) could be also considered as a factor preventing the grain boundary mobility and dislocation motion. Consequently, the grain refinement becomes more effective (Fig. 6a and c) and the structure is more strengthened, as shown by the microhardness values (Fig. 13), in the Cu-5Fe disc than in the pure Cu disc. The restriction of DRX in the Cu-5Fe disc may indicate that the Fe element decreases the stacking fault energy of the fabricated composite to some extent. Based on the microstructural analysis, it may be reasonably assumed that the combination of grain boundaries, dislocations, second phase particles and solute strengthening contributed to the strain hardening of the Cu-5Fe disc.

It is noted that the texture modification from the centre towards the mid-radius position was not drastic (see Fig. 11 a, c and e) when compared with the texture evolution of the HPT-processed Cu disc (see Fig. 10 a, c and e). It could be connected to the inhibited DRX process due to the addition of Fe elements since it was reported that the phase boundaries can delay the texture formation because of the deformation accommodation between the two phases [69]. The dominance of B/\bar{B} components with the presence of A_2^* or A_1^* components is frequently reported in materials with low stacking fault energies [46] which suggests that the Fe element may cause a decrease in the stacking fault energy of the Cu matrix.

The main characteristics of the deformation texture evolution in both consolidated discs are the deviations of the shear texture components from their ideal positions, especially at the mid-radius and edge positions. Moreover, it can be noted that the spread of some texture components like the A_2^* component in the HPT-processed Cu disc (see Fig. 10) and *B* component in the HPT-processed Cu-5Fe disc (see Fig. 11) may originate from the contribution of several causes simultaneously. Firstly, the deviation of shear texture components from their exact positions is attributed to the convergent/divergent nature of the lattice rotation field around the ideal positions [59, 70]. Secondly, the HPT processing was performed under quasi-constrained conditions, and thus, it is expected that there is some lengthening of the processed disc which caused the shift of the preferred orientations towards the shear direction [71]. In addition, it is highly probable that,

during the consolidation stage, the powder Cu and Fe particles have not been subjected to ideal shear deformation, leading to a deviation and the scattering of shear orientations [58].

Effect of annealing treatment on the consolidated discs

As expected, an annealing treatment at 500 °C for 6 h for the Cu and Cu-5Fe discs led to static recrystallization as manifest by grain growth (Figs. 4, 5 and 6) and decreasing microhardness values (Fig. 13b and d). In addition to static recrystallization, the annealed Cu-5Fe disc exhibits the precipitation of the Fe phase as confirmed by the XRD pattern (Fig. 2d), EBSD (see Fig. 7d-f) and STEM (see Fig. 9) results. However, the EBSD results suggest a dependency of static recrystallization behaviour on the measured position and the Fe element.

In the pure Cu disc, the annealed microstructure was reasonably similar across the disc diameter. The main microstructural characteristic of the annealed Cu disc is the presence of a high amount of Cu₂O oxide (see Fig. 4d-f) which mainly originates from contamination during the consolidation process. This suggests that the densification of the Cu powder was not completely achieved and this was apparent only after the annealing treatment which caused damage to the microstructure and mechanical properties by reducing the HAGBs fraction (~ 55%) and an associated increase in the inhomogeneity factor (see Table 4). Thus, it is concluded that it would be preferable to conduct the annealing treatments of the consolidated pure Cu discs under a protective argon atmosphere to reduce the impact of oxygen.

The texture of the Cu disc after annealing was principally retained except for a weakening of *B*-fibre and the formation of *A* and *A*₂^{*} components at the centre position, as shown in Fig. 10b, d and f. The occurrence of high DRX during deformation processing implies that all recrystallization nuclei exist already in the deformation state, as dynamically recrystallized grains or sub-grains, and the annealing treatment only provides the driving force for grain boundary migration. As a consequence, the deformation and recrystallization textures are similar. The development of a retained deformation texture is associated with the orientation growth theory [72, 73].

Regarding the annealed Cu-5Fe disc, the annealed microstructure (Fig. 5d, e and f), texture (Fig. 11b, d

and f) and microhardness (Fig. 13d) vary across the disc diameter. At the centre and mid-radius positions, a duplex microstructure develops (see Fig. 5d and e) due to the precipitation of Fe atoms from the Cu-rich matrix. Indeed, Fig. 9 demonstrates that, unlike the fine grains, the coarse grains were free from the Fe element. Due to the limited solubility of the Fe element in the Cu matrix according to the Cu-Fe phase diagram [30], the annealing treatment increases the diffusion process of the Fe element leading to the nucleation and growth of Fe grains. In addition, the introduction of large numbers of crystalline defects such as dislocations and vacancies owing to the high shear strain serves to promote the phase transformation by creating additional diffusion paths. Consequently, on one hand the pinning effect in the Cu grains is no longer present which allows the mobility of grain boundaries to be increased. On the other hand, the presence of Fe₃O₂ particles with different sizes (see Fig. 9) carried out sufficient pinning pressure to delay the grain boundary migration of the nano-sized grains. Despite the development of a heterogenous microstructure, the mechanical properties are more homogeneously distributed across the annealed disc diameter than in the HPT-processed disc, as demonstrated by the lowering of the *IF* factor after the annealing treatment (see Table 4). The improvement of the homogeneity could be attributed to the decrease of dislocation density and the formation of recrystallized grains. In fact, because of the heterogeneous nature of the microstructure (see Fig. 5), it is possible that the annealed Cu-5Fe disc exhibits a good strength-ductility combination. It is expected that the nano-sized grains provided the high strength while the elongation to failure would be supported through the coarse grains [16, 74].

Such heterogeneous microstructure is characteristic of an occurring discontinuous static recrystallization (DSRX), which includes the formation of nuclei of recrystallized grains and their consequent fast growth by grain boundary migration. This is known to follow the oriented nucleation theory [72, 73]. Usually, the occurrence of the DSRX mechanism in conventional deformed materials is accompanied by a noticeable change in the annealed texture [75, 76] which is in good agreement with the texture change observed at the centre and mid-radius positions (see Fig. 11). It is interesting to note that the texture modification after annealing occurred also in the Fe grains, as can be shown in Fig. 12. The strengthening

of J/\bar{J} components was reported in an HPT-processed and annealed Fe-9Cr (wt.%) alloy [77]. It was demonstrated that the J/\bar{J} oriented grains exhibit high stored energy and were surrounded by special grain boundaries which favour their recrystallization and their grain growth [77]. The coarse Cu grains at the mid-radius position were decorated by a high fraction of annealing twins (see Fig. 5e) which may be considered as an additional source for the texture modification. To confirm this proposal. Figure 15 shows an example of the RD-IPF maps superimposed

with HAGBs (black line) and twin boundaries (red line) of nano-sized and coarse Cu grains taken from the mid-radius position of the annealed Cu-5Fe disc (the RD-IPF map shown in Fig. 5e). First, the fraction of twins in the nano-sized grains is very low and they form a straight line (see white arrows) like a random grain boundary. The orientation of the nano-sized grains is dominated by the A_2^* component as demonstrated by the corresponding {111} pole figure.

By contrast, the fraction of annealing twins is visibly high in the coarse grains and exhibits a lamellar

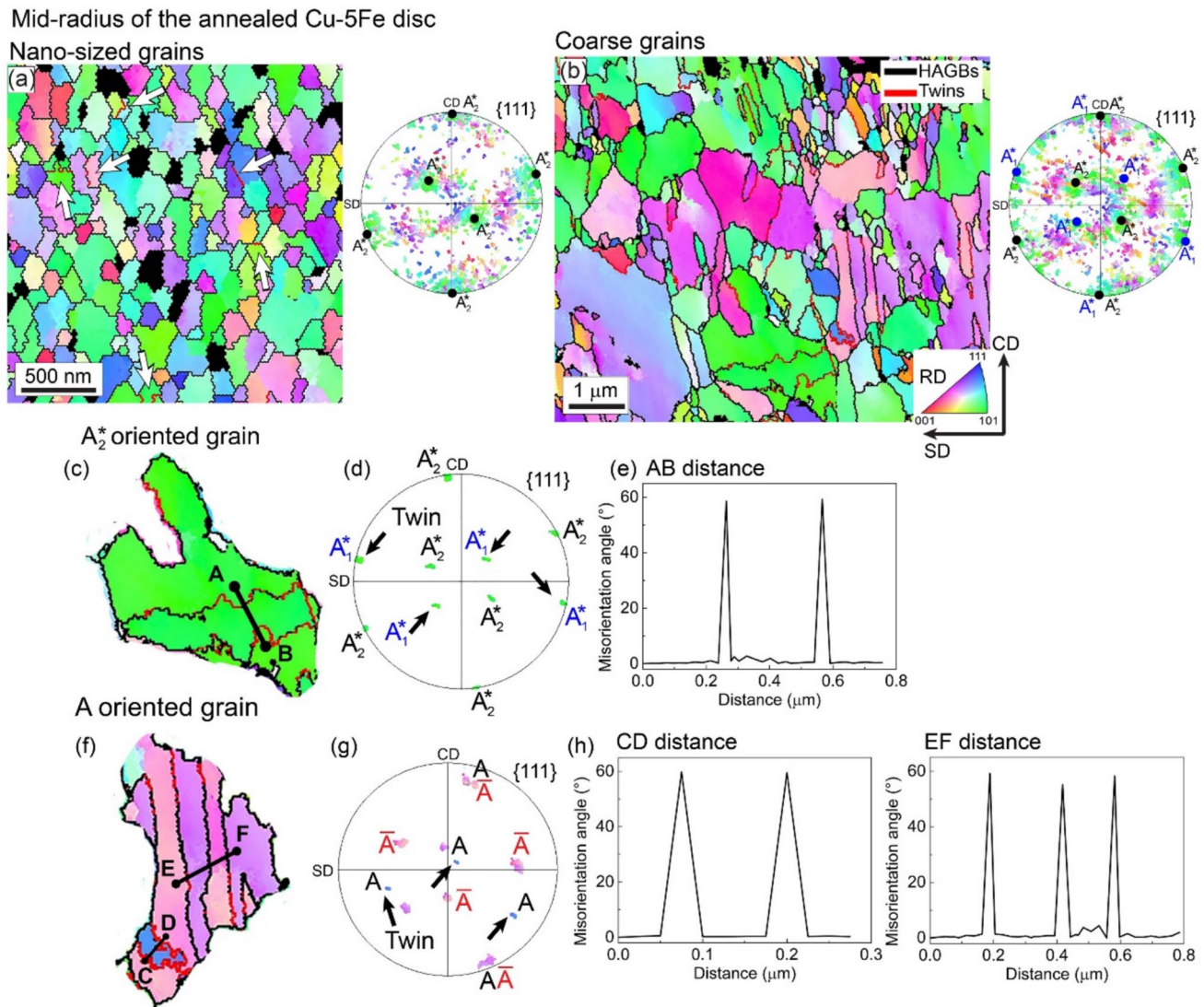


Figure 15 RD-IPF maps superposed with HAGBs and annealed twin boundaries and corresponding {111} pole figures of: **a** nano-sized and **b** coarse grains taken from the mid-radius position of the annealed Cu-5Fe disc (Fig. 5e). **c, f** example of A_2^* and A oriented grains, **d, g** {111} pole figures showing the orienta-

tion relationship between the parent A_2^* and A oriented grains and the twinned regions and **e, h** misorientation profiles corresponding to the AB distance in the A_2^* oriented grain, and CD and EF distances in the A oriented grain, respectively.

and band form. According to the corresponding {111} pole figure, the texture of these coarse grains is dominated by the A_2^* and A_1^* orientations.

In Fig. 15c and f, the isolated parent A_2^* and A oriented grains contain typical twin $\Sigma 3$ ($60^\circ < 111 >$) as demonstrated by the profile misorientation along the AB (see Fig. 15e) and CD (see Fig. 15h) distances, respectively. The isolated A oriented grain contains also several twins in the form of steps, as can be seen from the profile misorientation along the EF distance (see Fig. 15h).

The corresponding {111} pole figure reveals the crystallographic relationship between the parent A_2^* (Fig. 15d) and A (Fig. 15g) oriented grains and the twinned area. It is clear that the twining in the A_2^* and A oriented grains led to the formation of A_1^* and \bar{A} orientations, respectively, which explains their strengthening at the mid-radius position after the annealing treatment.

It is expected that the annealed microstructure at the mid-radius and edge positions will be similar since the average deformed grain size (Fig. 6c), the deformation texture (Fig. 11c and e), the microhardness (Fig. 13c) and the stored energy (Table 1) were similar. However, the present results demonstrate a good thermal stability of the edge position but with a net change in the texture evolution (see Fig. 5c and f). The uniform grain distribution after the annealing treatment is often associated with the continuous static recrystallization (CSRX) mechanism [78]. The CSRX mechanism applied the continuous transformation of sub-grains boundaries and LAGBs into HAGBs and this allows the production of a homogeneous microstructural evolution [78]. As shown in Fig. 6d, the fraction of HAGBs at the edge position was not changed after annealing (67% under deformation state vs. 65% under annealing state) since the HAGBs already formed during the HPT processing owing to the grain refinement. It is recognized that the transition from the DSRX to the CSRX mechanism is controlled by several parameters such as second particles, large strain and the critical fraction of HAGBs [75, 76, 79]. Based on the current microstructural evolution, the transition from the DSRX to the CSRX mechanism can be attributed to the difference in distribution and size of the Fe phase at the mid-radius and edge positions. Although the fraction of the Fe phase is similar ($\sim 4.0\%$), it is apparent that the Fe grains at the edge position are more refined (Table 2) and homogeneously dispersed (Fig. 7) within

the microstructure. Therefore, it is expected that the Cu/Fe grain interfaces delay the expansion of the two-phase grain boundaries which eventually prevent the grain growth of both the Fe and Cu grains.

In addition, the equivalent strain at the edge position ($\epsilon_{eq} = 815.7$) is almost ~ 2 times higher than in the mid-radius ($\epsilon_{eq} = 453.2$) position which increases the fraction of HAGBs from 61 to 67% leading to a more stable microstructure. This critical HAGBs value is consistent with previous investigations where it was found that the DSRX mechanism type dominated when the HAGBs fraction was less than 62% and the CSRX mechanism type was dominant if the HAGBs fraction was larger than 64% [75, 79]. Therefore, it is anticipated that it is necessary to obtain a deformation microstructure consisting of nano-sized grains with an HAGBs fraction of 67% in order to convert the annealed duplex microstructure into a uniform grain distribution.

Furthermore, the transition from the DSRX to the CDRX mechanism has a great impact on the annealed grain size (see Fig. 6c) but it appears to have little effect on the annealed texture evolution since at both positions the deformation texture changes into a complete A -fibre (see Fig. 11d and f). Generally, the deformation texture is retained during the occurrence of the CSRX mechanism [75, 76]. In the current research, regardless of the occurrence of the DSRX or CSRX mechanism, the texture change after annealing at both positions is a result of the restricted DRX and may be interpreted based on the oriented nucleation theory where the recrystallized texture arises from those nuclei which have the fastest growth rate in the deformed state [72].

A significant result is that the deformation textures in both the pure Cu and Cu-5Fe materials were different but ultimately they had similar textures after the annealing treatment. The partial A -fibre (A_1^*/A_2^* and A components with the absence of \bar{A} component) was developed during deformation processing in the Cu disc through DRX and this was retained after the annealing treatment. For the Cu-5Fe disc, the complete A -fibre (A_1^*/A_2^* and A/\bar{A} components) was developed only after annealing due to the restriction of the DRX process. Eventually, it can be concluded that the A -fibre is a stable texture in the consolidated Cu and Cu-5Fe discs. Nevertheless, some differences are noticed such as the development of the \bar{A} component and the strengthening of the annealed texture mainly due to the effect of the Fe addition (see Fig. 11d and f). Finally, it is noted that the

results demonstrate that the consolidated Cu-5Fe disc has a better thermal stability than the pure Cu disc.

Conclusions

The current investigation provides valuable insights into the deformation and static recrystallization behaviours of consolidated pure Cu and Cu-5Fe discs fabricated by HPT processing at RT through 30 turns. The main conclusions are as follows:

For the HPT-processed Cu disc, two grain refinement regimes were evident due to the accelerated DRX process leading to a grain size around 230 ± 15 nm and the formation of a partial *A*-fibre (A_1^*/A_2^* and *A* components with the absence of \bar{A} component). The formation of Cu_2O particles caused a serious oxidation problem during the annealing treatment, which inevitably affected the performance of the consolidated Cu disc. Despite this, the partial *A*-fibre persists after the annealing treatment.

For the HPT-processed Cu-5Fe disc, the DRX process was restricted so that there was more grain refinement (around 190 ± 20 nm) and a gradual shear texture formation in both the Cu and Fe grains. The CDRX and DDRX mechanisms simultaneously govern the grain refinement. The microhardness increased from the centre to the edge of the processed disc which caused a heterogeneous distribution of the mechanical properties. The HAGBs fraction and the precipitation of the Fe phase and its distribution during annealing treatment are responsible for the duplex microstructures at the centre and mid-radius positions and the stable microstructure at the edge position, respectively. Consequently, the transition from the DSRX to the CSRX mechanism was apparent across the annealed disc diameter. The presence of Fe_2O_3 oxide particles contributed to prevent grain growth. The restricted DRX process and annealing twins were responsible for the development of a recrystallization texture consisting of complete *A*-fibre (presence of A_1^*/A_2^* and A/\bar{A} components). The microhardness decreased due to the softening process and it was more homogeneously distributed across the disc diameter than the HPT-processed disc.

Acknowledgements

This research was partially supported by the PHC-Tassili program No. 24MDU114. National Science

Centre Poland provided funding for Dr P. Bazarnik under Grant Agreement No UMO-2024/53/B/ST11/00531.

Funding

PHC-Tassili program, No. 24MDU114, Hiba Azzedine, National Science Centre Poland, UMO-2024/53/B/ST11/00531, Piotr Bazarnik

Data availability

The datasets generated during the experiments and analysed under the current study are available from the corresponding authors upon reasonable request.

Declarations

Conflict of interest The authors declare no conflict of interest.

Ethical approval The authors have adhered to the accepted ethical standards of a genuine research study.

References

- [1] Wu Y, Zhang W, Li Y, Yang F, Liu H, Zou J, Jiang J, Fang F, Ma A (2024) An overview of microstructure regulation treatment of Cu-Fe alloys to improve strength, conductivity, and electromagnetic shielding. *J Alloys Compd* 1002:175425
- [2] Wang CP, Liu XJ, Kainuma R, Takaku Y, Ohnuma I, Ishida K (2004) Formation of core-type macroscopic morphologies in Cu-Fe base alloys with liquid miscibility gap. *Metal Mater Trans A* 35(4):1243–1253
- [3] Wang M, Yang Q-R, Jiang Y-B, Li Z, Xiao Z, Gong S, Wang Y-R, Guo C-L, Wei H-G (2021) Effects of Fe content on microstructure and properties of Cu-Fe alloy. *Trans Nonferrous Met Soc China* 31(10):3039–3049
- [4] Luo SB, Wang WL, Chang J, Xia ZC, Wei B (2014) A comparative study of dendritic growth within undercooled liquid pure Fe and Fe50Cu50 alloy. *Acta Mater* 69:355–364
- [5] Guo M, Wang F, Yi L (2016) The microstructure controlling and deformation behaviors of Cu-Fe-C alloy prepared by rapid solidification. *Mater Sci Eng, A* 657:197–209

[6] Zhang C, Chen C, Li P, Yan M, Qin Q, Yang F, Wang W, Guo Z, Volinsky AA (2022) Microstructure and properties evolution of rolled powder metallurgy Cu-30Fe alloy. *J Alloys Compd* 909:164761

[7] Liu KM, Lu DP, Zhou HT, Wen SF, Wei SY, Hu Q, Wan ZZ (2011) Microstructure and properties of Cu-17Fe alloy aged treatment in high magnetic field. *Adv Mater Res* 194–196:1270–1274

[8] Jo HR, Kim JT, Hong SH, Kim YS, Park HJ, Park WJ, Park JM, Kim KB (2017) Effect of silicon on microstructure and mechanical properties of Cu-Fe alloys. *J Alloys Compd* 707:184–188

[9] Jeong YB, Jo HR, Park HJ, Kato H, Kim KB (2020) Mechanical properties and microstructural change in (Cu-Fe) immiscible metal matrix composite: effect of Mg on secondary phase separation. *J Mater Res Technol* 9(6):15989–15995

[10] Zhang P, Lei Q, Yuan X, Sheng X, Jiang D, Li Y, Li Z (2020) Microstructure and mechanical properties of a Cu-Fe-Nb alloy with a high product of the strength times the elongation. *Mater Today Commun* 25:101353

[11] Yuan D, Liu Z, Guo C, Zeng H, Zhang J, Li M, Peng B, Yang B (2023) Effect of In on Fe phase morphology and properties of Cu-Fe alloy. *Mater Sci Technol* 39(18):3278–3287

[12] Zhang H, Zhang H, Li L (2009) Hot deformation behavior of Cu-Fe-P alloys during compression at elevated temperatures. *J Mater Process Technol* 209(6):2892–2896

[13] Dong Q, Shen L, Cao F, Jia Y, Liao K, Wang M (2015) Effect of thermomechanical processing on the microstructure and properties of a Cu-Fe-P alloy. *J Mater Eng Perform* 24(4):1531–1539

[14] Wang M, Jiang Y, Li Z, Xiao Z, Gong S, Qiu W, Lei Q (2021) Microstructure evolution and deformation behaviour of Cu-10 wt%Fe alloy during cold rolling. *Mater Sci Eng A* 801:140379

[15] Zhang C, Chen C, Huang L, Lu T, Li P, Wang W, Yang F, Volinsky AA, Guo Z (2021) Microstructure and properties of Cu-Fe alloys fabricated via powder metallurgy and rolling. *Powder Metall* 64(4):308–320

[16] Xu J, Guan B, Fu R, Wu Y, Hu Q, Zou J, Huang G, Yan C (2023) Tailoring the microstructure and mechanical properties of Cu-Fe alloy by varying the rolling path and rolling temperature. *J Mater Res Technol* 27:182–193

[17] Tian YZ, Yang Y, Peng SY, Pang XY, Li S, Jiang M, Li HX, Wang JW, Qin GW (2023) Managing mechanical and electrical properties of nanostructured Cu-Fe composite by aging treatment. *Mater Charact* 196:112600

[18] Xu J, Guan B, Fu R, Huang J, Liu W, Hu Q, Hu Z, Yan C (2024) The effect of multi-directional compression on mechanical properties and corrosion properties of Cu-Fe composite. *J Mater Res Technol* 28:1497–1503

[19] Lu D-P, Wang J, Zeng W-J, Liu Y, Lu L, Sun B-D (2006) Study on high-strength and high-conductivity Cu-Fe-P alloys. *Mater Sci Eng A* 421(1):254–259

[20] Edalati K, Bachmaier A, Beloshenko VA, Beygelzimer Y, Blank VD, Botta WJ, Bryla K, Čížek J, Divinski S, Enikeev NA, Estrin Y, Faraji G, Figueiredo RB, Fuji M, Furuta T, Grosdidier T, Gubicza J, Hohenwarter A, Horita Z, Huot J, Ikoma Y, Janeček M, Kawasaki M, Král P, Kuramoto S, Langdon TG, Leiva DR, Levitas VI, Mazilkin A, Mito M, Miyamoto H, Nishizaki T, Pippan R, Popov VV, Popova EN, Purcek G, Renk O, Révész Á, Sauvage X, Sklenicka V, Skrotzki W, Straumal BB, Suwas S, Toth LS, Tsuji N, Valiev RZ, Wilde G, Zehetbauer MJ, Zhu X (2022) Nanomaterials by severe plastic deformation: review of historical developments and recent advances. *Mater Res Lett* 10(4):163–256

[21] Zhilyaev AP, Langdon TG (2008) Using high-pressure torsion for metal processing: fundamentals and applications. *Prog Mater Sci* 53(6):893–979

[22] Edalati K, Ahmed AQ, Akrami S, Ameyama K, Aptukov V, Asfandiyarov RN, Ashida M, Astanin V, Bachmaier A, Beloshenko V, Bobruk EV, Bryla K, Cabrera JM, Carvalho AP, Chinh NQ, Choi I-C, Chulist R, Cubero-Sesin JM, Davdian G, Demirtas M, Divinski S, Durst K, Dvorak J, Edalati P, Emura S, Enikeev NA, Faraji G, Figueiredo RB, Floriano R, Fouladvind M, Fruchart D, Fuji M, Fujiwara H, Gajdics M, Gheorghe D, Gondek Ł, González-Hernández JE, Gornakova A, Grosdidier T, Gubicza J, Gunderov D, He L, Higuera OF, Hirosawa S, Hohenwarter A, Horita Z, Horky J, Huang Y, Huot J, Ikoma Y, Ishihara T, Ivanisenko Y, Jang J-I, Jorge AM, Kawabata-Ota M, Kawasaki M, Khelfa T, Kobayashi J, Kummel L, Korneva A, Kral P, Kudriashova N, Kuramoto S, Langdon TG, Lee D-H, Levitas VI, Li C, Li H-W, Li Y, Li Z, Lin H-J, Liss K-D, Liu Y, Cardona DMM, Matsuda K, Mazilkin A, Mine Y, Miyamoto H, Moon S-C, Müller T, Muñoz JA, Murashkin MY, Naeem M, Novelli M, Olasz D, Pippan R, Popov VV, Popova EN, Purcek G, de Rango P, Renk O, Retraint D, Révész Á, Roche V, Rodriguez-Calvillo P, Romero-Resendiz L, Sauvage X, Sawaguchi T, Sena H, Shahmir H, Shi X, Sklenicka V, Skrotzki W, Skryabina N, Staab F, Straumal B, Sun Z, Szczerba M, Takizawa Y, Tang Y, Valiev RZ, Vozniak A, Voznyak A, Wang B, Wang JT, Wilde G, Zhang F, Zhang M, Zhang P, Zhou J, Zhu X, Zhu YT (2024) Severe plastic deformation for producing superfunctional ultrafine-grained and heterostructured materials: an interdisciplinary review. *J Alloys Compd* 1002:174667

[23] Edalati K, Horita Z (2010) Application of high-pressure torsion for consolidation of ceramic powders. *Scr Mater* 63(2):174–177

[24] Bachmaier A, Pippan R (2019) High-pressure torsion deformation induced phase transformations and formations: new material combinations and advanced properties. *Mater Trans* 60(7):1256–1269

[25] Han J-K, Herndon T, Jang J-I, Langdon TG, Kawasaki M (2020) Synthesis of hybrid nanocrystalline alloys by mechanical bonding through high-pressure torsion. *Adv Eng Mater* 22(4):1901289

[26] Hernández-Escobar D, Kawasaki M, Boehlert CJ (2022) Metal hybrids processed by high-pressure torsion: synthesis, microstructure, mechanical properties and developing trends. *Int Mater Rev* 67(3):231–265

[27] Sauvage X, Wetscher F, Pareige P (2005) Mechanical alloying of Cu and Fe induced by severe plastic deformation of a Cu–Fe composite. *Acta Mater* 53(7):2127–2135

[28] Bachmaier A, Pippan R (2011) Microstructure and properties of a Fe–Cu composite processed by HPT powder consolidation. *Mater Sci Forum* 667–669:229–234

[29] Bachmaier A, Kerber M, Setman D, Pippan R (2012) The formation of supersaturated solid solutions in Fe–Cu alloys deformed by high-pressure torsion. *Acta Mater* 60(3):860–871

[30] Lukyanov A, Churakova A, Gunderov D, Filatov A, Antipov E, Situdikov V, Ganeev A, Valiev R, Pushin V (2016) Microstructure transformation in a cast Cu–Fe alloy at high pressure torsion deformation, *Rev. Adv. Mater. Sci.* 45(1-2):20-27.

[31] Stückler M, Krenn H, Kürnsteiner P, Gault B, De Geuser F, Weissitsch L, Wurster S, Pippan R, Bachmaier A (2020) Intermixing of Fe and Cu on the atomic scale by high-pressure torsion as revealed by DC- and AC-SQUID susceptometry and atom probe tomography. *Acta Mater* 196:210–219

[32] Asghari-Rad P, Choi YT, Nguyen NT-C, Sathiyamoorthi P, Kim HS (2021) Fabrication of layered Cu–Fe–Cu structure by cold consolidation of powders using high-pressure torsion. *J Korean Powder Metall Inst* 28(4):287–292

[33] Liu M, Zheng R, Li H, Wei Q, Ma C, Tsuji N (2024) Phase decomposition behavior and its impact on mechanical properties in bulk nanostructured Cu-20 at.%Fe supersaturated solid solution. *J Mater Sci Technol* 185:207–220

[34] Figueiredo RB, Cetlin PR, Langdon TG (2011) Using finite element modeling to examine the flow processes in quasi-constrained high-pressure torsion. *Mater Sci Eng A* 528(28):8198–8204

[35] Edalati K, Horita Z, Langdon TG (2009) The significance of slippage in processing by high-pressure torsion. *Scr Mater* 60(1):9–12

[36] Edalati K, Hashiguchi Y, Pereira PHR, Horita Z, Langdon TG (2018) Effect of temperature rise on microstructural evolution during high-pressure torsion. *Mater Sci Eng A* 714:167–171

[37] Huang Y, Sabbaghianrad S, Almazrouee AI, Al-Fadhalah KJ, Alhajeri SN, Langdon TG (2016) The significance of self-annealing at room temperature in high purity copper processed by high-pressure torsion. *Mater Sci Eng A* 656:55–66

[38] Cho J-H, Rollett AD, Oh KH (2005) Determination of a mean orientation in electron backscatter diffraction measurements. *Metall and Mater Trans A* 36(12):3427–3438

[39] Azzeddine H, Baudin T, Helbert A-L, Brisset F, Huang Y, Kawasaki M, Bradai D, Langdon TG (2021) A stored energy analysis of grains with shear texture orientations in Cu–Ni–Si and Fe–Ni alloys processed by high-pressure torsion. *J Alloys Compd* 864:158142

[40] Takayama Y, Szpunar JA, Kato H (2005) Analysis of intra-granular misorientation related to deformation in an Al–Mg–Mn alloy. *Mater Sci Forum* 495–497:1049–1054

[41] Hielscher R, Schaeben H (2008) A novel pole figure inversion method: specification of the MTEX algorithm. *J Appl Crystallogr* 41(6):1024–1037

[42] Andrzejczuk M, Siejka-Kulczyk J, Lewandowska M, Kurzydłowski KJ (2010) Microstructure investigations of dental composite samples prepared by focused ionbeam technique, *Journal of Microscopy* 237(3): 427–430

[43] Azzeddine H, Bourezg YI, Khereddine AY, Baudin T, Helbert AL, Brisset F, Kawasaki M, Bradai D, Langdon TG (2020) An investigation of the stored energy and thermal stability in a Cu–Ni–Si alloy processed by high-pressure torsion, *Philosophical Magazine* 100(6): 688–712

[44] Lee I, Bhatta L, Xu D, Blankenburg M, Lienert U, Liss K-D, Kawasaki M (2025) Defect-driven relaxation of nano-structured Cu examined by in situ heating high-energy synchrotron x-ray microbeam diffraction. *J Alloys Compd* 1028:180599

[45] Wongsa-Ngam J, Kawasaki M, Langdon TG (2013) A comparison of microstructures and mechanical properties in a Cu–Zr alloy processed using different SPD techniques. *J Mater Sci* 48(13):4653–4660

[46] Azzeddine H, Bradai D, Baudin T, Langdon TG (2022) Texture evolution in high-pressure torsion processing. *Prog Mater Sci* 125:100886

[47] Sadi S, Hanna A, Azzeddine H, Casas C, Baudin T, Helbert A-L, Brisset F, Cabrera JM (2021) Characterization of microstructure and texture of binary Mg–Ce alloy

processed by equal channel angular pressing. *Mater Charact* 181:111454

[48] Rafizadeh E, Mani A, Kazeminezhad M (2009) The effects of intermediate and post-annealing phenomena on the mechanical properties and microstructure of constrained groove pressed copper sheet. *Mater Sci Eng A* 515(1):162–168

[49] Kulagin R, Beygelzimer Y, Ivanisenko Y, Mazilkin A, Hahn H (2017) High pressure torsion: from laminar flow to turbulence. *IOP Conf Ser: Mater Sci Eng* 194(1):012045

[50] Wu Y-H, Bhatta L, Lee I, Figueiredo RB, Kawasaki M, Santala MK (2025) Multi-scale characterization of super-saturated and intermetallic nanoscale phases in alloys produced by high-pressure torsion processing of Al and Mg sheets. *JOM* 77(3):1233–1240

[51] Li X, Dippenaar RJ, Han J-K, Kawasaki M, Liss K-D (2019) Phase transformation and structure evolution of a Ti-45Al-7.5Nb alloy processed by high-pressure torsion. *J Alloys Compd* 787:1149–1157

[52] Kawasaki M, Han J-K, Liu X, Moon S-C, Liss K-D (2023) Synchrotron high-energy x-ray & neutron diffraction, and laser-scanning confocal microscopy: in-situ characterization techniques for bulk nanocrystalline metals. *Mater Trans* 64(8):1683–1694

[53] Wetscher F, Vorhauer A, Stock R, Pippian R (2004) Structural refinement of low alloyed steels during severe plastic deformation. *Mater Sci Eng A* 387–389:809–816

[54] Renk O, Pippian R (2019) Saturation of grain refinement during severe plastic deformation of single phase materials: reconsiderations, current status and open questions. *Mater Trans* 60(7):1270–1282

[55] Pippian R, Scheriau S, Taylor A, Hafok M, Hohenwarter A, Bachmaier A (2010) Saturation of fragmentation during severe plastic deformation. *Annu Rev Mater Res* 40:319–343

[56] Sakai T, Belyakov A, Kaibyshev R, Miura H, Jonas JJ (2014) Dynamic and post-dynamic recrystallization under hot, cold and severe plastic deformation conditions. *Prog Mater Sci* 60:130–207

[57] Khalfallah A, Azzeddine H, Baudin T, Brisset F, Huang Y, Langdon TG (2024) Texture and microstructural evolution in an Al-6061 alloy processed by high-pressure torsion. *Mater Charact* 212:114020

[58] Panda S, Toth LS, Zou J, Grosdidier T (2018) Effect of Strain Heterogeneities on Microstructure, Texture, Hardness, and H-Activation of High-Pressure Torsion Mg Consolidated from Different Powders, *Materials* 11(8): 1335

[59] Zhao Y, Massion R, Grosdidier T, Toth LS (2015) Gradient structure in high pressure torsion compacted iron powder. *Adv Eng Mater* 17(12):1748–1753

[60] Zhao YJ, Massion R, Grosdidier T, Toth LS (2014) Contribution of shear deformation to grain refinement and densification of iron powder consolidated by high pressure torsion. *IOP Conf Ser: Mater Sci Eng* 63(1):012032

[61] Yavari AR, Desré PJ, Benameur T (1992) Mechanically driven alloying of immiscible elements. *Phys Rev Lett* 68(14):2235–2238

[62] Tóth LS, Neale KW, Jonas JJ (1989) Stress response and persistence characteristics of the ideal orientations of shear textures. *Acta Metall* 37(8):2197–2210

[63] Liao XZ, Zhao YH, Srinivasan SG, Zhu YT, Valiev RZ, Gunderov DV (2004) Deformation twinning in nanocrystalline copper at room temperature and low strain rate. *Appl Phys Lett* 84(4):592–594

[64] Heye W, Wasserman G (1968) The formation of the rolling textures in FCC metals by slip and twinning. *Scripta Metall* 2(4):205–207

[65] dos Santos IC, Mazzer EM, Figueiredo RB, Langdon TG, Pereira PHR (2023) Evidence for two-stage hardening in an Al-Zn-Mg-Cu alloy processed by high-pressure torsion. *J Alloy Compd* 941:168839

[66] Al-Fadhalah KJ, Alhajeri SN, Almazrouee AI, Langdon TG (2013) Microstructure and microtexture in pure copper processed by high-pressure torsion. *J Mater Sci* 48(13):4563–4572

[67] Ekiz EH, Lach TG, Averbach RS, Mara NA, Beyerlein IJ, Pouryazdan M, Hahn H, Bellon P (2014) Microstructural evolution of nanolayered Cu–Nb composites subjected to high-pressure torsion. *Acta Mater* 72:178–191

[68] Khereddine AY, Hadj Larbi F, Azzeddine H, Baudin T, Brisset F, Helbert A-L, Mathon M-H, Kawasaki M, Braudai D, Langdon TG (2013) Microstructures and textures of a Cu–Ni–Si alloy processed by high-pressure torsion. *J Alloys Compd* 574:361–367

[69] Xu J, Peng Y, Guan B, Xin Y, Chapuis A, Huang G, Liu Q (2022) Tailoring the microstructure and texture of a dual-phase Mg–8Li alloy by varying the rolling path. *Mater Sci Eng A* 844:143202

[70] Baczynski J, Jonas JJ (1996) Texture development during the torsion testing of α -iron and two IF steels. *Acta Mater* 44(11):4273–4288

[71] Beyerlein IJ, Tóth LS (2009) Texture evolution in equal-channel angular extrusion. *Prog Mater Sci* 54(4):427–510

[72] Doherty RD (1985) Nucleation and growth kinetics of different recrystallization texture components. *Scripta Metall* 19(8):927–930

[73] Schmidt U, Lücke K (1979) Recrystallization textures of silver copper and α -brasses with different zinc-contents as a function of the rolling temperature. *Texture Stress Microstruct* 3(2):146381

[74] Cheng Z, Bu L, Zhang Y, Wu H, Zhu T, Lu L (2023) Characterization of gradient plastic deformation in gradient nanotwinned Cu. *Acta Mater* 246:118673

[75] Jazaeri H, Humphreys FJ (2004) The transition from discontinuous to continuous recrystallization in some aluminium alloys: II – annealing behaviour. *Acta Mater* 52(11):3251–3262

[76] Jazaeri H, Humphreys FJ (2004) The transition from discontinuous to continuous recrystallization in some aluminium alloys: I – the deformed state. *Acta Mater* 52(11):3239–3250

[77] Duan J, Wen H, Zhou C, Islamgaliev R, Li X (2019) Evolution of microstructure and texture during annealing in a high-pressure torsion processed Fe-9Cr alloy. *Materialia* 6:100349

[78] Doherty RD, Hughes DA, Humphreys FJ, Jonas JJ, Jensen DJ, Kassner ME, King WE, McNelley TR, McQueen HJ, Rollett AD (1997) Current issues in recrystallization: a review. *Mater Sci Eng A* 238(2):219–274

[79] Ashby MF, Humphreys FJ, Sellar CM, Shercliff HR, Stowell MJ, Humphreys FJ, Prangnell PB, Bowen JR, Ghosh A, Harris C (1999) Developing stable fine-grain microstructures by large strain deformation. *Philos Trans R Soc Lond Ser A Math Phys Eng Sci* 357(1756):1663–1681

Publisher's Note Springer Nature remains neutral with regard to jurisdictional claims in published maps and institutional affiliations.

Springer Nature or its licensor (e.g. a society or other partner) holds exclusive rights to this article under a publishing agreement with the author(s) or other rightsholder(s); author self-archiving of the accepted manuscript version of this article is solely governed by the terms of such publishing agreement and applicable law.